CaV1 and CaV2 calcium channels mediate the release of distinct pools of synaptic vesicles

Brian D. Mueller[1#], Sean A. Merrill[1#], Shigeki Watanabe[2,3], Ping Liu[4], Anish Singh[1], Alex Cherry[1], Malan Silva[1,6], Zhao-Wen Wang[4], Erik M. Jorgensen[1,5*]

[1] Department of Biology, University of Utah, Salt Lake City, UT
[2] Department of Cell Biology, John Hopkins University, Baltimore, MD
[3] Solomon H. Snyder Department of Neuroscience, John Hopkins University, Baltimore, MD
[4] Department of Neuroscience, University of Connecticut Medical School, Farmington, CT
[5] Howard Hughes Medical Institute, University of Utah, Salt Lake City, UT
[6] Human Technopole Foundation, Milan, Italy
[*] Lead contact
[#] Authors contributed equally towards this work

Abstract

Activation of voltage-gated calcium channels at synapses leads to local increases in calcium and the fusion of synaptic vesicles. However, presynaptic output will be determined by the density of calcium channels, the dynamic properties of the channel, the distance to docked vesicles, and the release probability at the docking site. We demonstrate that at *C. elegans* neuromuscular junctions, CaV2, and CaV1 mediate the release of two distinct pools of synaptic vesicles. Superresolution microscopy demonstrates that CaV2 channels are concentrated in densely packed clusters ~300 nm in diameter with active zone proteins Neurexin, α-Liprin, SYDE, ELKS, RIMB, α-Catulin, and MAGI. The CaV2 channels mediate the fusion of vesicles docked within 100 nm of the dense projection and is colocalized with to the synaptic vesicle priming protein UNC-13L. By contrast, CaV1 channels are dispersed in the synaptic varicosity and are coupled to internal calcium stores via the ryanodine receptor. The CaV1 and ryanodine receptor mediate the fusion of vesicles docked broadly in the synaptic varicosity and are colocalized with the vesicle priming protein UNC-13S. These distinct synaptic vesicle pools, released by different calcium channels, could be used to tune the speed, voltage-dependence, and quantal content of neurotransmitter release.

Introduction

Presynaptic boutons have an intricate molecular architecture that determines their activity during synaptic transmission (Ackermann, Waites, & Garner, 2015; Haucke, Neher, & Sigrist, 2011). The site of vesicle fusion in the presynaptic bouton, called the active zone, is directly opposed to the ligand-gated ion channels in the postsynaptic membrane. Within the active zone, scaffolding proteins interact with transsynaptic adhesion molecules and recruit voltage-gated calcium channels (Südhof, 2012). Synaptic vesicles are tethered, docked and primed at release sites in the active zone by Unc13 proteins (Neher & Brose, 2018). The coupling of calcium channels to release sites will determine the transfer function of synapses to depolarizing inputs (Eggermann, Bucurenciu, Goswami, & Jonas, 2012; Eguchi, Montanaro, le Monnier, & Shigemoto, 2022; Özçete & Moser, 2021; Rebola et al., 2019). Transfer will depend on the dynamic properties of the calcium channel, the concentration of calcium at the release site, and the release probability of the vesicle.

Voltage-gated calcium channels can be divided into three molecular families: CaV1, CaV2, and CaV3, each with fundamentally different properties including voltage-sensitive activation and inactivation (Catterall, Perez-Reyes, Snutch, & Striessnig, 2005; Dolphin, 2021; Dolphin & Lee, 2020). These classes are primarily associated with tissue-specific functions: In muscle, CaV1 (L-type) channels mediate contraction and are coupled to internal calcium stores

via the ryanodine receptor (RyR). In neurons, CaV2 (P/Q, N, and R-type) channels drive synaptic transmission. In neurons and excitable cells, CaV3 (T-type) regulate action potential oscillations and pacemaker frequencies (Dolphin, 2021). These tissue-specific roles are not exclusive, for example, CaV1 variants are associated with neurotransmitter release in hair cells (CaV1.3) and photoreceptors (CaV1.4) (Dolphin & Lee, 2020).

In the nematode *C. elegans*, each class is encoded by a single gene: CaV1 (*egl-19*), CaV2 (*unc-2*), CaV3 (*cca-1*), and RyR (*unc-68*). In both vertebrates and *C. elegans*, CaV2 is the main calcium channel for synaptic transmission (J E Richmond, Weimer, & Jorgensen, 2001; R W Tsien, Lipscombe, Madison, Bley, & Fox, 1988; Richard W Tsien & Tsien, 1990). Nematodes lack voltage-gated sodium channels and neurotransmission is mediated via graded release (Ping Liu, Chen, & Wang, 2014; Qiang Liu, Hollopeter, & Jorgensen, 2009), and the frequency of tonic miniature currents ('minis') is severely reduced in *unc-2* mutants, but some release remains (J E Richmond et al., 2001; Tong et al., 2017). Physiological studies suggest CaV1 can also contribute to neurotransmission; CaV1 channel blockers reduce tonic minis (Tong et al., 2017). However, the role of CaV1 channels at synapses is complicated because CaV1 also contributes to calcium-mediated action potentials in the worm (Qiang Liu, Kidd, Dobosiewicz, & Bargmann, 2018). Finally, the ryanodine receptor also contributes to neurotransmission, and is specifically required for multivesicular release (Chen et al., 2017; Qiang Liu et al., 2005).

The calcium signal will rapidly dissipate by diffusion. Intracellular calcium is extremely low (0.05 μM), and levels required for fusion relatively high (half-maximal 10 μM) (Courtney, Briguglio, Bradberry, Greer, & Chapman, 2018; Schneggenburger & Neher, 2000). Free calcium will be further depleted by calcium buffers and calcium pumps (Blaustein, 1988; Eggermann et al., 2012). The effective range of calcium around a single voltage-gated calcium channel is calculated to be only 20 nm for evoked fusion, a 'nanodomain' approximately the diameter of the calcium channel itself (Fedchyshyn & Wang, 2005; Weber et al., 2010). For synapses to reliably track high frequency action potentials, there must be a large number of channels to negate the stochastic nature of channel opening, and the channels must be tightly coupled to the release sites in this nanodomain. Thus, the transfer function not only depends on the identity of the calcium channel, but also depends on the density of calcium channels and the distance to the docked vesicle. By contrast, at some synapses calcium 'microdomains' can drive synaptic vesicle fusion, 80-200 nm from the calcium channels (Eggermann et al., 2012; Vyleta & Jonas, 2014) suggesting that some calcium signals are more robust and do not require tight physical coupling. The tuning of the output of the presynapse then ultimately depends on the

organization of calcium channels and the proteins that dock vesicles (Eggermann et al., 2012; Nakamura et al., 2015).

Vesicle docking and priming at the active zone is mediated by Unc13 homologs (Dittman, 2019; Neher & Brose, 2018). Unc13 tethers vesicles to the active zone by membrane interactions of the C2B and C2C domains independent of SNARE proteins (Imig et al., 2014; Quade et al., 2019). The MUN domain interacts with the SNARE protein syntaxin (Augustin, Rosenmund, Südhof, & Brose, 1999; Lai et al., 2017; Yang et al., 2015) and promotes the open state of Unc13 to allow SNARE protein interactions (J E Richmond et al., 2001). Mutants lacking Unc13 fail to dock and prime synaptic vesicles in worms and in mice (Hammarlund, Palfreyman, Watanabe, Olsen, & Jorgensen, 2007; Imig et al., 2014; Janet E Richmond, Davis, & Jorgensen, 1999; Siksou et al., 2009). Unc13 proteins have two structural isoforms (UNC-13L and UNC-13S in *C. elegans*), which differ by the presence or absence of the C2A domain at the N-terminus(Dittman, 2019). The active zone protein RIM interacts with the C2A domain to inhibit homodimerization and activates Unc13 in both vertebrates and worms (Betz et al., 2001; Hu, Tong, & Kaplan, 2013; H. Liu et al., 2019; Lu et al., 2006; Zhou, Stawicki, Goncharov, & Jin, 2013). The Unc13 isoforms that lack the C2A domain are associated with ELKS proteins in mice and flies (Böhme et al., 2016; Kawabe et al., 2017).

Here, we demonstrate using electrophysiology in *C. elegans* that two different classes of voltage-gated calcium channels, CaV2 (UNC-2) and CaV1 (EGL-19) mediate the release of two distinct pools of synaptic vesicles. A third calcium channel, the ryanodine receptor (RyR, UNC-68), functions with CaV1 in vesicle release. Time-resolved electron microscopy in genetic mutants demonstrates that CaV2 fuses synaptic vesicles at the dense projection of the active zone and CaV1 and RyR fuse vesicles at lateral sites. Finally, we use super-resolution fluorescence microscopy to demonstrate that CaV2 is localized with UNC-13L at the dense projection, and that CaV1 and RyR colocalize with UNC-13S at distal sites. Altogether, we describe two essential pools of synaptic vesicles: (1) the central pool is localized adjacent to the dense project, vesicles are docked by UNC-13, and released by a dense cluster of CaV2 channels. (2) The lateral pool of vesicles is broadly distributed, docked by UNC-13S, and released by dispersed CaV1 and RyR channels.

Results

Two independent calcium sources at presynapses

The genome of *C. elegans* contains only a single gene for each major voltage-gated calcium channel class: CaV1 (*egl-19*), CaV2 (*unc-2*), CaV3 (*cca-1*), and a single calcium-gated

RyR (*unc-68*), referred to by common name hereafter. Loss of the CaV3 T-type channel does not affect neurotransmitter release in acetylcholine neurons (H. Liu et al., 2018), so we investigated null mutations in CaV1, CaV2, and RyR. Null mutants lacking CaV2 (*unc-2*(*lj1)*) and RyR (*unc-68*(*e540*)) are viable, but CaV1 (*egl-19*(*st556)*) die as embryos due to a loss of muscle function (Lee, Lobel, Hengartner, Horvitz, & Avery, 1997). Expression of CaV1 using a muscle-specific promoter rescues viability, hereafter this strain is described as the nervous system null 'CaV1(Δns)'. This strain can be fully rescued with the addition of a nervous system rescue of CaV1.

To determine whether the channels function cooperatively or in parallel, we generated double mutant combinations of the three channel types. The double mutant lacking CaV1(Δns) and RyR is viable, and is no worse than the RyR null, consistent with their coupled function. However, loss of CaV2 with either CaV1 or with RyR resulted in a synthetic lethal interaction (Table S1). These data suggest that calcium influx from CaV2 acts redundantly and in parallel to a CaV1-RyR calcium source during neurotransmission. To bypass synthetic lethal interactions, we rescued viability by expressing CaV2 using a promoter specific for head acetylcholine neurons (P*unc-17*h)(Hammarlund et al., 2007; Topalidou et al., 2016), suggesting worm viability requires a few acetylcholine neurons in the head neuropil. This strain lacks CaV2 calcium channels in the motor neurons of the ventral nerve cord, hereafter referred to as CaV2(Δnmj). Expression of CaV2 in the head restored viability in double mutants with CaV1 or with RyR. These double mutants exhibit a synthetic paralyzed phenotype. This restoration of viability confirms that the lethality of the CaV2 and CaV1 or RyR genetic interaction is due to disrupted neuronal function.

CaV2 or CaV1 and ryanodine receptor synaptic vesicle pools

To confirm disrupted neuronal function in calcium channel double mutants, we directly assayed postsynaptic currents using electrophysiology recordings from body muscle. Miniature postsynaptic currents ('minis') are caused by the release of neurotransmitter from one or a few synaptic vesicles (Chen et al., 2017; Q. Liu, 2005). The nematode neuromuscular junction releases neurotransmitter via graded release (Ping Liu et al., 2014; Qiang Liu et al., 2009) and the burst of minis drives calcium action potentials in the muscles (P. Liu et al., 2011). The rate of miniature postsynaptic currents (mPSCs) compared to the wild type (32.5 +/- 3.5 minis/s) is reduced by ~40% in CaV2 (18.7 +/- 3.9 minis/s), CaV1 (21.2 +/-2.8 minis/s), and RyR (20.4 +/- 3.5 minis/s) single mutants (Figure 1A). The rate of minis in the CaV1(Δns) RyR double mutant is similar to each single mutant (19.6 +/- 2 mini/s), supporting the interdependent relationship of these two channels. The mini rates of CaV2(Δnmj) CaV1(Δns) double mutants (12.8 +/- 2.4

mini/s) and CaV2(Δnmj) RyR double mutants (11.3 +/- 2.1 mini/s) are significantly diminished, but not completely abolished. This lingering neuronal activity in these strains is likely due to CaV2 expression from head-rescued CaV2 neurons synapsing onto the muscles (the sublateral cord motor neurons) or from low-level expression in the ventral cord motor neurons.

To determine if CaV1 and CaV2 are required for all neurotransmitter release, we blocked CaV1 acutely using nemadipine (Kwok et al., 2006). Miniature currents in wild-type worms were reduced by 43% when treated with nemadipine (untreated: 32.5 +/- 3.5 minis/s; nemadipine: 18.4 +/- 2 minis/s). In CaV2(-) null animals, nemadipine almost completely abolished mini frequency (1.7 +/- 0.6 mini/s). In contrast, nemadipine did not change mini frequency in either the CaV1(Δns) mutant (20.4 +/- 2.5 mini/s) or the RyR(-) mutant (20.7 +/- 1.3 mini/s) (Figure 1B). We conclude that CaV2(Δnmj) is expressed at low levels at neuromuscular junctions and that all neurotransmitter release at these neuromuscular junctions relies on CaV1 and CaV2. The mean amplitude of the miniature currents is similar to the wild type in the absence of CaV1 or CaV2 indicating that these mutants do not affect either vesicle size or the postsynaptic receptor function (Extended Data Figure 1A-D). As previously reported, the mean amplitude of the RyR loss-of-function mutant is decreased (16.0 +/- 1.8 pA). To determine if this reduction was from defects in multiquantal release, the mode, or peak value of the miniature current amplitudes after 1pA binning was taken. The mode values which likely represent single vesicle fusions, were similar in all genotypes (WT: 10 pA; CaV2 8pA, CaV1Δns 10pA, RyR 8pA, CaV2Δnmj/RyR 10pA, CaV2Δnmj/CaV1Δns 12pA, CaV1Δns/RyR 10pA) (Extended Data Figure 1E-F), suggesting that internal calcium stores are required for multiquantal events (Chen et al., 2017; Qiang Liu et al., 2005). Together, these data demonstrate that CaV2 and CaV1 / RyR channels regulate the release of separate synaptic vesicle pools at neuromuscular junctions.

CaV2 and CaV1 mediate fusion of separate pools of synaptic vesicles

The physiology data suggest that CaV2 and CaV1 mediate the release of distinct synaptic vesicle pools at the same synapse. To demonstrate these calcium channels regulate synaptic vesicle fusion, “flash-and-freeze” time-resolved electron microscopy was used to characterize fusing vesicle pools (Watanabe et al., 2013). Transgenic animals expressing channelrhodopsin in acetylcholine neurons were loaded into a high-pressure freezing chamber, and stimulated with a 20-ms light pulse to depolarize neurons and activate synaptic calcium channels. Animals were frozen 50 ms after stimulation; control animals were treated identically but not stimulated. Frozen samples were fixed by freeze substitution, embedded in plastic and sectioned for electron microscopy (Watanabe et al., 2013). Docked vesicles are defined as those in contact with the plasma membrane; docking was segmented blind to treatment and

genotype (Figure 2A,B). The distance to the closest dense projection was plotted on the X-axis (Figure 2C). Decreases in docked vesicles after stimulation were assumed to be the result of synaptic vesicle fusion, although calcium influx could cause some vesicles to undock and return to the cytoplasm (Kusick et al., 2020)

To identify vesicle fusions associated with particular calcium channels, we analyzed the distribution of docked vesicles in mutant animals. In unstimulated animals, docked vesicles are clustered around dense projections, although many are observed at lateral regions extending beyond 100 nm from dense projections. Docked vesicles are uniformly depleted after stimulation in wild-type animals (Figure 2D). Genetic ablation of CaV2 channels reduced vesicle fusions adjacent to the dense projection; docked vesicles distal to the dense projection still fused in response to stimulation (Figure 2E). Mutation of the CaV1 channel reduced fusion broadly, although significant vesicle fusions were observed within 100 nm of the dense projection (Figure 2F). Similar to CaV1 mutants, absence of RyR exhibited vesicle fusions adjacent to the dense projection but reduced fusions greater than 100 nm from the dense projection (Figure 2G). For these experiments we used the CaV1 hypomorph *egl-19(n582)* and the CaV1 CaV2 double mutant *egl-19(n582) unc-2(lj1)* is viable. The double mutant of synaptic vesicles after stimulation (Figure 2H). These data demonstrate that *C. elegans* neuromuscular junctions have two spatially distinct pools of synaptic vesicles: a central pool dependent on CaV2 calcium channels and a lateral pool dependent on CaV1 and RyR.

CaV2 and CaV1 are segregated at synapses

The electron microscopy data suggests that CaV1 and CaV2 are localized to spatially separate areas of the active zone. To localize calcium channels at synapses at physiological conditions we tagged the endogenous genes and localized them using fluorescence microscopy. We performed 3-color imaging using dense projection markers as an anatomical fiducial at the center of the synapse. Because *C. elegans* synaptic varicosities are less than 1µm in diameter, super-resolution microscopy was required to resolve channel clusters. A small segment of the dorsal nerve cord, where neuromuscular junctions exist, was imaged, and the region of imaging was restricted to a narrow band to avoid potential complications by the signal from CaV1 expression in muscle. To ensure that the pattern of synapses in our fluorescence images matched the arrangement of neuromuscular junctions, we reconstructed 20 µm of the dorsal cord. All imaging was conducted on living, acutely anesthetized nematodes.

Multiple tagging sites were tested for all genes, but in some cases the tags disrupted function, or the splice isoforms were not expressed in neurons. For all voltage gated calcium

channels internal sites within regions of poor conservation were successfully modified (Extended Figure 2A-C). CaV2 was tagged with HALO (Grimm, Brown, English, Lionnet, & Lavis, 2017) in the second extracellular loop near the N-terminus (Kurshan et al., 2018; Schwartz & Jorgensen, 2016).

To confirm that the pattern of calcium channels in our fluorescence images matched the arrangement of dense projections in electron micrographs, we reconstructed 20 µm of the dorsal nerve cord from serial sections (Figure 3A). CaV2 clusters are localized every 1.10 +/- 0.16 µm along the dorsal cord, and echoes the distribution of dense projections in the reconstruction (1.02 / µm). To identify proteins associated with CaV2, we tagged multiple active zone components implicated in scaffolding and release complexes at the dense projection (Ackermann et al., 2015; Südhof, 2012). Neurexin (*nrx-1*), Magi (*magi-1*), Syde1 (*syd-1*), Liprin-α (*syd-2*), RIMBP (*rimb-1*), and α-Catulin (*ctn-1*) were tagged with Skylan-S. Each of these proteins is closely associated with CaV2::HALO puncta (Figure 3B).

In particular, ELKS form distinct, highly punctate clusters at similar intervals along the dorsal cord (1.03 +/- 0.04 µm), and are reliably associated with CaV2 clusters (Figure 3C). ELKS serves as a synaptic fiducial for CaV2 and CaV1 comparisons. To quantify the distribution of CaV2 relative to ELKS, an axis was determined using the two cluster centers, and CaV2 localization displacements along the axis to the ELKS cluster center were measured and plotted as a histogram (Figure 3D). The 95% confidence interval of these distance measurements will be called the “diameter” of the cluster. CaV2 clusters are larger, 297 nm in diameter, and often encompass the ELKS cluster (294nm); 62% of ELKS localizations are within a CaV2 cluster (Figure 4A-C). The CaV2 cluster center is slightly offset from the ELKS cluster (124nm), which may be due to the positions of the tags on their respective proteins, or because CaV2 and ELKS tags are on opposites sides of the plasma membrane.

In contrast to the highly concentrated subsynaptic CaV2 distribution, CaV1 was distributed mainly as dispersed tiny puncta, further away from the synaptic marker ELKS and CaV2 (center to center 262nm), was broadly distributed (diameter 869 nm) (Figure 4A,B), and shares only a 24% overlap with ELKS (Figure 4C). A similar distribution was observed when CaV1 distribution was measured relative to CaV2, with 24% of CaV1 localizations within the CaV2 distribution (Figure 4C). This suggests CaV1 is not paired with the dense projection, instead distributed laterally in the active zone.

CaV1 is highly expressed in the muscle, to confirm that the CaV1 localizations are

presynaptic and not in the muscle or hypoderm, we generated a HALO-tagged CaV1 under the pan-neuronal synaptotagmin promotor (P*snt-1*) in the CaV1(Δns) strain, which fully rescued function (Extended Data 1G). For ease of genetic crosses, we used RIM binding-protein (RIMBP/RIMB-1) as a dense projection marker. The overexpressed CaV1::HALO tended to be more punctate than the endogenously tagged protein (Ext Data Figure 3A,B). However, CaV1 was not colocalized with RIMBP and the distances between clusters similar to the endogenously tagged gene (center-to-center endogenous CaV1 tag: 262nm; P*snt-1:*CaV1 tag: 378 nm)(Extended Data 3E). To demonstrate that CaV1 clusters are presynaptic we expressed LIN-7 / VELI, a potential CaV1 channel scaffold through PDZ domain interactions (Butz, Okamoto, & Südhof, 1998; Pym et al., 2017), in acetylcholine motor neurons (Extended Data 3C,D). CaV1 and LIN-7 clusters were closely associated, but not associated with RIMBP (Extended Data 3E). These data suggest that CaV1 is localized at presynaptic boutons in a separate domain from CaV2 channels.

If CaV1 and RyR function in the same vesicle fusion pathway, they must be colocalized (Piggott & Jin, 2021). RyR was tagged with HALO at the N-terminus of the neuronal isoform (Extended Data Figure 2C) (Marques et al., 2020). RyR localizations were compared to CaV1 localizations and a dense projection marker, in this case neurexin (NRX-1::Skylan-s) for convenience of genetic crosses (Figure 5A,B). RyR localizations were diffusely distributed, and lateral to the dense projection (peak-to-peak 393nm; 25 synapses) (Figure 5C). RyR localizations were tightly correlated with CaV1. 94% of RyR localizations are within 100nm of a CaV1 localization (Figure 5D). CaV1 exhibited a slightly broader distribution; nevertheless, 82% of CaV1 localizations are within 100nm of a RyR channel (Figure 5D). The spatial correlation between CaV1 and RyR are consistent with functional interactions at lateral sites independent of CaV2 clusters.

Different UNC-13 isoforms are associated with CaV1 and CaV2

Vesicle docking and SNARE priming requires UNC-13 proteins. Null mutations in *unc-13* nearly eliminate neurotransmission and vesicle docking in *C. elegans* (Hammarlund et al., 2007; Janet E Richmond et al., 1999). We edited the *unc-13* locus at the C-terminus to add Skylan-S to label all splice isoforms (UNC-13all)(Extended Data 2D). UNC-13all was tightly associated with calcium channels (Figure 6A-C). A high percentage of total UNC-13all localizations were found within 100nm of CaV2 and CaV1 (92% and 97%, respectively) by nearest-neighbor analysis (Figure 6D).

The short isoform UNC-13S lacks the C2A domain, which is required to bind to RIM, has

a diffuse distribution at synapses (Hu et al., 2013; Weimer et al., 2006; Zhou et al., 2013) UNC-13S was edited at its unique N-terminus with Skylan-S. UNC-13S does not colocalize with CaV2 (peak-to-peak 319nm) but is associated with CaV1 (Figure 7A-C). Nearest neighbor analysis indicates that 99% of UNC-13S localizations are within 100nm of a CaV1 (Figure 7D), demonstrating that a specialized isoform of UNC-13 docking machinery is localized to CaV1 calcium channels.

Discussion

Calcium channel classes tend to be associated with specific tissue functions: CaV2 (N, P/Q, R-type) with synaptic transmission, and CaV1 (L-type) channels with muscle contraction. Here, we demonstrate that both CaV2 and CaV1 channels drive vesicle fusion at *C. elegans* neuromuscular junctions and mediate the release of different synaptic vesicle pools. In electrophysiological assays, these pools are genetically separable and perfectly complementary. Electron microscopy using flash-and-freeze stimulation demonstrated that CaV2 channels fuse vesicles near the dense projection, whereas CaV1 channels drove vesicle fusion at lateral sites in the same synapses. Super-resolution imaging indicates that CaV2 channels are tightly associated with the active zone proteins Neurexin, α-Liprin, ELKS, RIMBP. In addition, CaV2 is associated with the long isoform of the docking and priming protein UNC-13L. By contrast, CaV1 is dispersed in the synaptic varicosity and is associated with the short isoform UNC-13S. Finally, the localization and functions of CaV1 in synaptic transmission are spatially and functionally coupled to the ryanodine receptor, which regulates calcium release from internal stores (Figure 8).

CaV1 functions at synapses

In *C. elegans* there is only a single L-type channel, encoded by the *egl-19* gene and primarily plays a role in muscle development and contraction (Lee et al., 1997). Recent data suggests that EGL-19 can also generate calcium action potentials in some neurons (Qiang Liu et al., 2018), and thereby substitute for the absence of voltage-gated sodium channels in nematodes. However, L-type channel inhibitors do not affect evoked release in the worm, but rather decrease spontaneous fusions (Tong et al., 2017). We demonstrate that null mutations in *egl-19* have reduced rates of tonic miniature currents, are presynaptically localized, and are involved in fusions of a specific sub-pool of synaptic vesicles. Together these data suggest that this L-type channel is acting to mediate fusion of synaptic vesicles.

The participation of the CaV1 L-type channel EGL-19 in synaptic transmission in *C. elegans* is unusual but not unprecedented. L-type channels were originally characterized as

339 muscle calcium channels. However, CaV1 channels also play a primary role in synaptic vesicle
340 fusion at graded sensory synapses: CaV1.3 drives neurotransmission in hair cells and CaV1.4
341 acts at ribbon synapses in photoreceptors (Schmitz & Witkovsky, 1997; S. Y. Zhang, Robertson,
342 Yates, & Everett, 1999). CaV1.2 and CaV1.3 are also expressed broadly in the brain and
343 function in dendritic spines during synaptic plasticity (Hell et al., 1996, 1993; Nanou & Catterall,
344 2018), although possible presynaptic roles remain largely unexplored.
345
346 **Multiple calcium channels - coupling and voltage-dependence**
347 Although based on the physiological data alone, it was possible that CaV1 and CaV2
348 channels were functioning at separate synapses, the electron microscopy and fluorescence
349 experiments demonstrate that these channels are functioning at the same synaptic varicosity.
350 Participation of multiple classes of calcium channels at the same synapse could tune the
351 dynamics of neurotransmission. Differences in voltage-dependent activation, inactivation,
352 clustering, or distance to docked vesicles could regulate synchronous or asynchronous release
353 (Dolphin, 2021).
354
355 One important difference is that CaV1 channels inactivate more slowly than CaV2
356 channels (Naranjo, Wen, & Brehm, 2015; Yu, Yuan, Westenbroek, & Catterall, 2018). CaV1.3
357 and CaV1.4 mediate graded release in auditory hair cells and photoreceptors, respectively.
358 Slow inactivation of these channels enables graded neurotransmitter release (McRory et al.,
359 2004; Platzer et al., 2000). The *C. elegans* CaV1 channel EGL-19 also exhibits slow inactivation
360 *in vivo* (Lainé, Ségor, Zhan, Bessereau, & Jospin, 2014), which likely contributes to tonic
361 miniature currents (H. Liu et al., 2018). These attributes may also terminate neurotransmission
362 in motor neurons; calcium influx through EGL-19 is specifically coupled to repolarization via
363 SLO-2 BK potassium channels (Ping Liu et al., 2014).
364
365 The most profound difference observed at *C. elegans* neuromuscular junctions is that
366 they are differentially localized: CaV2 is localized to a large cluster at the dense projection,
367 CaV1 is distributed broadly in the synapse. Vesicle pools can be assayed as tightly coupled or
368 loosely coupled to calcium channels based on sensitivity to EGTA (Dittman & Ryan, 2019;
369 Eggermann et al., 2012). At *C. elegans* neuromuscular junctions, UNC-13L mediates tight
370 coupling (EGTA-insensitive), whereas UNC-13S mediates loose coupling (EGTA-sensitive) (Hu
371 et al., 2013). Consistent with these findings, our data indicate UNC-13L is localized to dense
372 projections along with potentially dozens of CaV2 channels. The CaV2 channel mediates the
373 release of vesicles tightly associated with the dense projection, but cannot fuse vesicles greater
374 than 100 nm from the dense projection. In contrast to CaV2, CaV1 channels are dispersed

375 across the synapse and frequently at solitary localizations. Nevertheless, CaV1 channels can
376 drive fusion of a very large distribution of docked vesicles, extending 500 nm from the dense
377 projection.
378
379 **RyR**
380 The requirement of CaV1 for the fusion of this distal pool of vesicles is likely to be
381 mediated by the ryanodine receptor rather than by CaV1 directly. Calcium influx from CaV1
382 channels stimulates the release of calcium from the endoplasmic reticulum via the ryanodine
383 receptor (Bouchard, Pattarini, & Geiger, 2003). In skeletal muscle, CaV1.1 is physically coupled
384 to RyR1 and voltage-sensing by the calcium channel can gate the ryanodine receptor in the
385 absence of extracellular calcium (Schneider, 1994). In neurons, it is unclear if CaV1 channels
386 are physically coupled to RYRs. In *C. elegans*, there is no physical link between CaV1 and the
387 RyR since depolarizations in the absence of calcium do not elicit synaptic vesicle release (Q.
388 Liu, 2005). Data demonstrated here indicate a spatial and functional link. Nearest neighbor
389 analysis indicates that essentially all RyR localizations are within 100 nm of a CaV1 channel,
390 and the electrophysiology and electron microscopy demonstrate that they mediate fusion of the
391 same pool of vesicles. Ryanodine receptors are also found at vertebrate presynapses
392 (Bouchard et al., 2003); further work is required to demonstrate a role for ryanodine receptors in
393 synaptic vesicle release at vertebrate synapses.
394
395 **Summary**
396 In summary, we find that different classes of calcium channels CaV2 and CaV1
397 colocalized with different isoforms of docking and priming proteins, UNC-13L and UNC-13S,
398 respectively, at the *C. elegans* neuromuscular junction. These proteins are localized at different
399 sites and mediate fusion of different pools of synaptic vesicles.
400
401 Cooperation between calcium channel classes may be widespread. Immunofluore-
402 scence experiments indicate that both CaV1 and CaV2 channels are localized together at the
403 same neuromuscular junctions in the fly (Krick et al., 2021). Beyond invertebrates, mouse CaV1
404 and CaV2 channels function together at neuromuscular junctions (Katz, Ferro, Weisz, & Uchitel,
405 1996; Urbano & Uchitel, 1999) Finally, pharmacological experiments suggest that CaV1 and
406 CaV2 channels function together in GABA neurons in the central nervous system (Goswami,
407 Bucurenciu, & Jonas, 2012; Rey et al., 2020). Recent work indicates that CaV1 channels and
408 RyR2 function together and colocalize at junctions in the cell body of hippocampal neurons
409 (Sahu et al., 2019). It is likely that CaV1 mediates ryanodine receptor function at vertebrate
410 synapses as well. Finally, the presence of analogous isoforms the UNC-13 proteins, Munc13-1

411 and bMunc13-2, function together at the same synapses, suggest that this organization of
412 synapses into separately regulated pools of synaptic vesicles may be general.
413

Methods

Rescue of Lethal Calcium Channel Mutants

Lethal CaV1/*egl-19*(st556) animals were rescued by Mos-mediated transgenes (Frøkjær-Jensen et al., 2014, 2008). An *egl-19* minigene was constructed from cDNA and portions of gDNA containing small unconserved introns to aid expression. The first exons 1-4 are cDNA, followed by gDNA of exon 5-9, and cDNA of exon 10-17. The minigene was placed downstream from a muscle P*set-18* promoter and inserted directly into the genome by MosSCI (Frøkjær-Jensen et al., 2008). The resulting construct oxTi1047 was crossed into CaV1/*egl-19*(st556) bearing animals. A second copy of the *egl-19* minigene was placed after a neuronal P*snt-1* promoter and carried into the genome by miniMos (Frøkjær-Jensen et al., 2014). The resulting oxTi1049 construct was crossed into the muscle-rescued CaV1/*egl-19*(st556) animals.

Lethal double mutants of CaV2-RyR (*unc-2* lj1;*unc-68* e540) and CaV2-CaV1(*unc-2* lj1;*egl-19* st556) were rescued by an extrachromosomal array expressing SNAP::CaV2/*unc-2* cDNA in a minimum set of acetylcholine head neurons, using a previously described truncated *unc-17* promoter (Hammarlund et al., 2007; Topalidou et al., 2016). The array oxEx2096 was generated in *unc-2*(lj1) strain AQ130 and crossed to RyR/*unc-68*(e540) or CaV1/*egl-19*(st556);oxTi1047 bearing animals. The resulting strains are lethal without the presence of oxEx2096[P*unc-17*::*SNAP*::*unc-2*] and were used in electrophysiology experiments.

Generation of CaV2::HALO by CRISPR/cas9

CaV2 was tagged by CRISPR-mediated insertion of HALO coding DNA into the *unc-2* endogenous genomic locus. A DNA mix containing 1) PCR-generated DNA repair template that includes the HALO tag with an embedded Cbr-unc-119(+) cassette flanked by loxP sites and 33bp homology arms to the cut site, 2) plasmid DNA that directs expression of Cas9 and an sgRNA (Schwartz & Jorgensen, 2016), and 3) an inducible negative selection plasmid directing expression of a histamine-gated chloride channel in neurons, pNP403 (Pokala, Liu, Gordus, & Bargmann, 2014) was injected into the gonads of young adult EG6207[*unc-119(ed3)*] animals (Maduro & Pilgrim, 1995; Schwartz & Jorgensen, 2016; X. Zhang et al., 2015). Transgenic animals were selected for expression of unc-119(+), and extrachromosomal-array bearing animals were selected against by addition of histamine to the media. The loxP::Cbr-unc-119(+)::loxP region of the insertion was excised by injecting pDD104[Peft-3::Cre]and identifying unc-119(-) animals (Dickinson, Ward, Reiner, & Goldstein, 2013). The modified locus introduces HALO-tag within an unconserved region in the second extracellular loop of CaV2 encoding UNC-2a. The resulting strain EG9823[*unc-119*(ed3); *unc-2*(ox672[HALO])] was subsequently used to generate CRISPR-mediated insertions of SKYLAN-S tags.

Generation of Super-Resolution Tags by CRISPR/cas9

Tags for other genes, including *egl-19, unc-68, elks-1, nrx-1, rimb-1, elks-1, syd-2, syd-1, magi-1, ctn-1, unc-13,* and *unc-13b* were constructed as previously described (Schwartz & Jorgensen, 2016). A single plasmid containing sgRNA and the repair template, composed of 57bp homology arms and SKYLAN-S (X. Zhang et al., 2015) containing a loxP::*Cbr-unc-119*(+)::loxP, was appended by SapTrap plasmid assembly. Each assembled plasmid was mixed with plasmids to express Cas9 in the germline, and HisCl- in neurons, and injected into the gonads of young adult EG9823 animals. After selecting for unc-119(+) and selecting against extrachromosomal arrays by histamine application, animals were injected with pDD104[Peft-3::Cre], selected for excision of loxP::*Cbr-unc-119*(+)::loxP, and outcrossed once before analysis by super-resolution microscopy.

Strains:

All strains were maintained at 22C on standard NGM media seeded with OP50.

Electrophysiology strains

N2 (wild-type).

EG9034: *oxTi1047[Pset-18::egl-19b::let-858 3'utr] II; egl-19(st556)*

AQ130: *unc-2(lj1) X*

CB540: *unc-68(e540) V*

EG9405: *unc-68(e540) V; unc-2(lj1) X; oxEx2097[Punc-17h::SNAP::unc-2]*

EG9406: *unc-2(lj1) oxTi1047[Pset-18::egl-19b::let-858 3'utr] II; egl-19(st556)IV; unc-2(lj1) X; oxEx2097[Punc-17h::SNAP::unc-2]*

EG8827: *egl-19(st556)IV; unc-68(e540) V; oxTi1047[Pset-18::egl-19b::let-858 3'utr] II;*

Electron microscopy strains

EG5793: *oxSi91[Punc-17::ChIEF::mCherry::unc-54UTR unc-119(+) II; unc-119(ed9) III*

EG6584: *oxSi91[Punc-17::ChIEF::mCherry::unc-54UTR unc-119(+) II; unc-2(lj1) X*

EG6586: *oxSi91[Punc-17::ChIEF::mCherry::unc-54UTR unc-119(+) II; egl-19(n582) IV; unc-2(lj1) X.*

EG6587: *oxSi91[Punc-17::ChIEF::mCherry::unc-54UTR unc-119(+) II; unc-68(e540) V*

EG6585: *oxSi91[Punc-17::ChIEF::mCherry::unc-54UTR unc-119(+) II; egl-19(n582) IV*

Single molecule localization strains

EG9823: u*nc-2(ox672[HALO::unc-2]) X unc-119(ed3) III*

EG9617: *elks-1(ox747[skylan-s]), egl-19(ox728[SNAP]) IV; unc-2(ox672[HALO]) X*

EG9667: *egl-19(ox728[SNAP]), elks-1(ox747[skylan-s]) IV unc-68(ox721[HALO]) V*

EG9722: *unc-2(ox672[HALO]) X; egl-19(ox728[SNAP]) IV; unc-44(ox802[skylan-s]) IV*

EG9418: *egl-19(st556) IV; ox704[skylan-s::rimb-1] III; oxTi1047[Pset-18::egl-19b::let858utr; HygroR(+)] II; oxTi1055[Psnt-1::HALO::egl-19b; NeoR(+)] II; unc-44(ox708[unc-44::snap]) IV*

EG10094: *oxTi1055[Psnt-1::HALO::egl-19b; NeoR(+)] oxTi1047[Pset-18::egl-19b::let858utr; HygroR(+)] II ; unc-119(ed3) III rimb-1(ox704[skylan-s]) III ; egl-19(st556) IV ; oxEx2223[Punc-129::lin-7::SNAPf]*

EG9723: *unc-2(ox672[HALO]) X; egl-19(ox728[SNAP]) IV; unc-13(ox748[skylan-s]) I*

EG9782: *unc-13(ox814[SKYLAN-S(loxP)]) I; unc-2(ox672[HALO]) X; egl-19(ox728[SNAP]) IV*

EG9588: *egl-19(ox728[SNAP]) IV nrx-1(ox719[skylan-s]) V unc-2(ox672[HALO]) X*

EG9475: *oxIs322[CB-unc-119(+) Pmyo-2::mCherry::histone Pmyo-3::mCherry::histone] II unc-119(ed3) III; rimb-1(ox704[skylan-s]) III; egl-19(ox728[snap]) IV unc-2(ox672[HALO::]) X*

EG9476: *ctn-1d(ox727[skylan-s]) I; oxIs322[CB-unc-119(+) Pmyo-2::mCherry::histone Pmyo-3::mCherry::histone] II; unc-119(ed3) III; egl-19(ox728[SNAP]) IV; unc-2(ox672[HALO]) X*

EG9425: *unc-119(ed3) III; unc-2(ox672[HALO]), syd-2(ox715[skylan-s(loxP::Runc-119::loxP)]) X*

EG10095: *syd-1(ox723[skylan-s(loxP::Runc-119::loxP)]) II; unc-119(ed3) III; unc-2(ox672[HALO]) X*

EG10096: *unc-119(ed3) III; egl-1-19(ox728[snap]), magi-1(ox755[skylan-s(loxP::Rcb-unc-119::loxP)]) IV; unc-2(ox672[HALO]) X*

Single Molecule Localization Microscopy

Super-resolution images were recorded with a Vutara SR 352 (Bruker Nanosurfaces, Inc., Madison, WI) commercial microscope based on single molecule localization biplane technology (Juette et al., 2008; Mlodzianoski, Juette, Beane, & Bewersdorf, 2009). *C. elegans* expressing HALO- tagged proteins (Encell, 2013; Mollwitz et al., 2012) were stained for two hours in 50µM of HTL-JF646, and 50µM of STL-JF549cp, STL-JF549, or STL-JF549pa (Gift from Luke Lavis, Janelia Farms; (Grimm et al., 2017, 2015)). Early super-resolution experiments were conducted with JF549-STL or PA-JF549-STL, we later found that a new cell permeable variant cp-JF549-STL improved labeling of channels. Animals were recovered 12 hours at 15degC on agar seeded with OP50 bacteria. Live intact animals were anesthetized in 25mM NaN3 and regions of their dorsal cords that were positioned directly against the cover glass and away from the intestine were imaged with 640nm excitation power of 10kW/cm2, or 549nm excitation power of 5kW/cm2 SKYLAN-S was imaged by 488nm excitation at 2kW/cm2, while photoactivated by 0.37mW/cm2 405nm light. Images were recorded using a 60x/1.2 NA Olympus water immersion objective and Hamamatsu Flash4 V1 sCMOS, or 60x/1.3 NA Silicon immersion objective and

Orca Fusion BT SCMOS camera with gain set at 50 and frame rate at 50 Hz. Data was analyzed by the Vutara SRX software (version 7.0.0rc39). Single molecules were identified by their brightness frame by frame after removing the background. Identified molecules were localized in three dimensions by fitting the raw data in a 12x12-pixel region of interest centered around each particle in each plane with a 3D model function that was obtained from recorded bead data sets. Fit results were filtered by a density based denoising algorithm to remove isolated particles. The experimentally achieved image resolution of 40nm laterally (x,y) and 70 nm axially (in z) was determined by Fourier ring correlation. Localizations were rendered as 80nm.

SML Analysis

Localization data was exclusively collected from the dorsal nerve cord, which contains axons and synapses but no neuronal soma. We performed a 3D reconstruction of C. elegans dorsal nerve cord to inform region of interest selection from fluorescent images. The orientation of dorsal cord synapses is predictable. Excitatory acetylcholine neurons and inhibitory GABA neurons synapse onto muscle arms (Figure 3A). These connections are near the edges of the cord bundle. Thus, the roll of the animal affects the orientation of the synapse; en face or axial.

For single molecule localization experiments, animals were rolled to ensure en face orientation of synapses. Synapses that were in focus and en face were analyzed. The average size of a synapse from the dorsal nerve cord is 579.7nm (SEM +/- 16nm). Thus, super-resolution analysis regions of interest were narrowed to localizations within 700nm of the dense projection marker. Localization position data was flattened in the z-dimension due to chromatic aberrations. A script was used to calculate the center of each probe. To compare the distribution of probe A to probe B, an angle between the two clusters centers was calculated. The distribution distances were calculated by measuring the distance along the center-to-center axis from a probe B to the center of cluster A, and cluster B. Nearest neighbor analysis was done with knnsearch. Distribution center and range or “diameter” were reported as (mean , 95%CI).

Electrophysiology

All electrophysiological experiments were completed with young adult hermaphrodites. The animals were immobilized and dissected as previously described (Ping Liu, Chen, Mailler, & Wang, 2017). Worm preparation was bathed with an extracellular solution containing (in mM) NaCl 140, KCl 5, CaCl2 0.5, MgCl2 5, dextrose 11 and HEPES 5 (pH 7.2). Spontaneous postsynaptic currents (PSCs) at neuromuscular junction were recorded at a holding voltage of -60 mV with a pipette solution containing (in mM) NaCl 140, KCl 5, CaCl2 5, MgCl2 5, dextrose 11 and HEPES 5 (pH 7.2). The classic whole-cell recordings were performed with a Multiclamp

700B amplifier (Molecular Devices, Sunnyvale, CA, USA) and the Clampex software (version 10, Molecular Devices). Data were filtered at 2 kHz and sampled at 10 kHz. Nemadipine-A (Sigma-Aldrich) was first dissolved in DMSO to make frozen stock solution (10mM), and was diluted to a final concentration of 10 µM in extracellular solution before use. Animals were treated for 5 minutes. The frequency and amplitude of minis were quantified with MiniAnalysis (Synaptosoft, Decatur, GA, USA). The amplitudes of evoked currents were quantified using Clampfit (version 10, Molecular Devices, Sunnyvale, CA, USA)

Flash and Freeze Electron Microscopy

Electron microscopy was performed as previously described (Watanabe et al., 2013). Freezing was performed on a Leica EMpact2 (Leica, Wetzlar, Germany). To stimulate neurotransmission animals were exposed to blue (488nm) LED light for 20ms and frozen 50ms later. 33nm serial sections were taken and imaged using a Hitachi H-7100 transmission electron microscope equipped with a Gatan Orius digital camera (Gatan, Pleasanton, CA). Micrographs were analyzed in ImageJ using a program for morphological analysis of synapses (Watanabe, Davis, Kusick, Iwasa, & Jorgensen, 2020). Scripts available at: https://github.com/shigekiwatanabe/SynapsEM

Dorsal Nerve Cord Reconstruction

100nm thickness serial sections were imaged using JEOL JEM-1400 (JEOL, Peabody, MA) then annotated and assembled using TrackEM2 in FIJI (Cardona et al., 2012). Specifically, a wireframe was fit through each process that was suspected to be in the previous micrograph. Then an outline of the plasma membrane of each process was drawn. We analyzed several criteria to more specifically determine the specific process name and type: the morphology of each process and compared to previously published data (J.G. White, E. Southgate, J.N. Thomson, & S. Brenner, 1986), and the number of synapses. These data allow us to determine the identity of a process with some certainty.

Acknowledgements

We thank Lexy von Diezmann for development of Proberuler. We thank Luke Lavis for providing all Janelia Fluor dyes (JF Dyes). We thank the Caenorhabditis Genetics Center (CGC) for maintaining and distributing strains to the *C. elegans* community. We thank Patrick McEachern, Matthew Rich, Jessica Vincent and M. Wayne Davis for their critical reviews of this manuscript. EMJ is an investigator at Howard Hughes Medical Institute.

FUNDING

Erik Jorgensen

National Science Foundation NeuroNex 2014862

National Institute of Health NIH NINDS 5R01NS034307

Sean Merrill

NIH F31 NRSA Predoctoral Fellows grant #1F31NS084826

Zhao-wen Wang

National Institute of Health NIH R01MH085927 and R01NS109388

Author Contributions

BDM SAM EMJ Wrote manuscript

SAM SW BDM EMJ Designed experiments

SW SAM EMJ Conceived of the project

PL Performed electrophysiology

SAM BDM Performed single molecule localization microscopy

BDM LVD designed Proberuler

BDM SAM Analyzed single molecule localization data

SAM AC Performed genetic crosses

SAM AC BDM cloned plasmids

SAM BDM Generated transgenic animals

SW Performed and analyzed time resolved electron microscopy

BDM AS MS annotated serial reconstruction

MS Performed serial reconstruction electron microscopy

References

Ackermann, F., Waites, C. L., & Garner, C. C. (2015). Presynaptic active zones in invertebrates and vertebrates. *EMBO Reports*, *16*(8). https://doi.org/10.15252/embr.201540434

Augustin, I., Rosenmund, C., Südhof, T. C., & Brose, N. (1999). Munc13-1 is essential for fusion competence of glutamatergic synaptic vesicles. *Nature*, *400*(6743), 457–461. https://doi.org/10.1038/22768

Betz, A., Thakur, P., Junge, H. J., Ashery, U., Rhee, J.-S., Scheuss, V., … Brose, N. (2001). Functional Interaction of the Active Zone Proteins Munc13-1 and RIM1 in Synaptic Vesicle Priming. *Neuron*, *30*(1), 183–196. https://doi.org/https://doi.org/10.1016/S0896-6273(01)00272-0

Blaustein, M. P. (1988). Calcium transport and buffering in neurons. *Trends in Neurosciences*, *11*(10), 438–443. https://doi.org/https://doi.org/10.1016/0166-2236(88)90195-6

Böhme, M. A., Beis, C., Reddy-Alla, S., Reynolds, E., Mampell, M. M., Grasskamp, A. T., … Sigrist, S. J. (2016). Active zone scaffolds differentially accumulate Unc13 isoforms to tune Ca2+ channel–vesicle coupling. *Nature Neuroscience*, *19*(10), 1311–1320. https://doi.org/10.1038/nn.4364

Bouchard, R., Pattarini, R., & Geiger, J. D. (2003). Presence and functional significance of presynaptic ryanodine receptors. *Progress in Neurobiology*, *69*(6), 391–418. https://doi.org/https://doi.org/10.1016/S0301-0082(03)00053-4

Butz, S., Okamoto, M., & Südhof, T. C. (1998). A Tripartite Protein Complex with the Potential to Couple Synaptic Vesicle Exocytosis to Cell Adhesion in Brain. *Cell*, *94*(6), 773–782. https://doi.org/https://doi.org/10.1016/S0092-8674(00)81736-5

Cardona, A., Saalfeld, S., Schindelin, J., Arganda-Carreras, I., Preibisch, S., Longair, M., … Douglas, R. J. (2012). TrakEM2 Software for Neural Circuit Reconstruction. *PLoS ONE*, *7*(6), e38011. https://doi.org/10.1371/journal.pone.0038011

Catterall, W. A., Perez-Reyes, E., Snutch, T. P., & Striessnig, J. (2005). International Union of Pharmacology. XLVIII. Nomenclature and Structure-Function Relationships of Voltage-Gated Calcium Channels. *Pharmacological Reviews*, *57*(4), 411. https://doi.org/10.1124/pr.57.4.5

Chen, B., Liu, P., Hujber, E. J., Li, Y., Jorgensen, E. M., & Wang, Z.-W. (2017). AIP limits neurotransmitter release by inhibiting calcium bursts from the ryanodine receptor. *Nature Communications*, *8*(1), 1380. https://doi.org/10.1038/s41467-017-01704-z

Courtney, N. A., Briguglio, J. S., Bradberry, M. M., Greer, C., & Chapman, E. R. (2018). Excitatory and Inhibitory Neurons Utilize Different Ca(2+) Sensors and Sources to Regulate Spontaneous Release. *Neuron*, *98*(5), 977-991.e5. https://doi.org/10.1016/j.neuron.2018.04.022

Dickinson, D. J., Ward, J. D., Reiner, D. J., & Goldstein, B. (2013). Engineering the Caenorhabditis elegans genome using Cas9-triggered homologous recombination. *Nature Methods*, *10*(10), 1028–1034. https://doi.org/10.1038/nmeth.2641

Dittman, J. S. (2019). Unc13: a multifunctional synaptic marvel. *Current Opinion in Neurobiology*, *57*, 17–25. https://doi.org/https://doi.org/10.1016/j.conb.2018.12.011

Dittman, J. S., & Ryan, T. A. (2019). The control of release probability at nerve terminals. *Nature Reviews Neuroscience*, *20*(3), 177–186. https://doi.org/10.1038/s41583-018-0111-3

Dolphin, A. C. (2021). Functions of Presynaptic Voltage-gated Calcium Channels. *Function*, *2*(1), zqaa027. https://doi.org/10.1093/function/zqaa027

Dolphin, A. C., & Lee, A. (2020). Presynaptic calcium channels: specialized control of synaptic neurotransmitter release. *Nature Reviews Neuroscience*, *21*(4), 213–229. https://doi.org/10.1038/s41583-020-0278-2

Eggermann, E., Bucurenciu, I., Goswami, S. P., & Jonas, P. (2012). Nanodomain coupling between Ca2+ channels and sensors of exocytosis at fast mammalian synapses. *Nature Reviews Neuroscience*, *13*(1), 7–21. https://doi.org/10.1038/nrn3125

Eguchi, K., Montanaro, J., le Monnier, E., & Shigemoto, R. (2022). The Number and Distinct Clustering Patterns of Voltage-Gated Calcium Channels in Nerve Terminals. *Frontiers in*

669 *Neuroanatomy*, *16*. Retrieved from
670 https://www.frontiersin.org/article/10.3389/fnana.2022.846615
671 Encell, L. P. (2013). Development of a Dehalogenase-Based Protein Fusion Tag Capable of
672 Rapid, Selective and Covalent Attachment to Customizable Ligands. *Current Chemical*
673 *Genomics*, *6*(1), 55–71. https://doi.org/10.2174/1875397301206010055
674 Fedchyshyn, M. J., & Wang, L.-Y. (2005). Developmental Transformation of the Release
675 Modality at the Calyx of Held Synapse. *The Journal of Neuroscience*, *25*(16), 4131.
676 https://doi.org/10.1523/JNEUROSCI.0350-05.2005
677 Frøkjær-Jensen, C., Davis, M. W., Sarov, M., Taylor, J., Flibotte, S., LaBella, M., … Jorgensen,
678 E. M. (2014). Random and targeted transgene insertion in Caenorhabditis elegans using a
679 modified Mos1 transposon. *Nature Methods*, *11*(5), 529–534.
680 https://doi.org/10.1038/nmeth.2889
681 Frøkjær-Jensen, C., Wayne Davis, M., Hopkins, C. E., Newman, B. J., Thummel, J. M., Olesen,
682 S.-P., … Jorgensen, E. M. (2008). Single-copy insertion of transgenes in Caenorhabditis
683 elegans. *Nature Genetics*, *40*(11), 1375–1383. https://doi.org/10.1038/ng.248
684 Goswami, S. P., Bucurenciu, I., & Jonas, P. (2012). Miniature IPSCs in Hippocampal Granule
685 Cells Are Triggered by Voltage-Gated Ca²⁺ Channels via
686 Microdomain Coupling. *The Journal of Neuroscience*, *32*(41), 14294.
687 https://doi.org/10.1523/JNEUROSCI.6104-11.2012
688 Grimm, J. B., Brown, T. A., English, B. P., Lionnet, T., & Lavis, L. D. (2017). *Synthesis of*
689 *Janelia Fluor HaloTag and SNAP-Tag Ligands and Their Use in Cellular Imaging*
690 *Experiments*. https://doi.org/10.1007/978-1-4939-7265-4_15
691 Grimm, J. B., English, B. P., Chen, J., Slaughter, J. P., Zhang, Z., Revyakin, A., … Lavis, L. D.
692 (2015). A general method to improve fluorophores for live-cell and single-molecule
693 microscopy. *Nature Methods*, *12*(3), 244–250. https://doi.org/10.1038/nmeth.3256
694 Hammarlund, M., Palfreyman, M. T., Watanabe, S., Olsen, S., & Jorgensen, E. M. (2007). Open
695 Syntaxin Docks Synaptic Vesicles. *PLOS Biology*, *5*(8), e198-. Retrieved from
696 https://doi.org/10.1371/journal.pbio.0050198
697 Haucke, V., Neher, E., & Sigrist, S. J. (2011). Protein scaffolds in the coupling of synaptic
698 exocytosis and endocytosis. *Nature Reviews Neuroscience*, *12*(3), 127–138.
699 https://doi.org/10.1038/nrn2948
700 Hell, J. W., Westenbroek, R. E., Breeze, L. J., Wang, K. K., Chavkin, C., & Catterall, W. A.
701 (1996). N-methyl-D-aspartate receptor-induced proteolytic conversion of postsynaptic class
702 C L-type calcium channels in hippocampal neurons. *Proceedings of the National Academy*
703 *of Sciences*, *93*(8), 3362–3367. https://doi.org/10.1073/pnas.93.8.3362
704 Hell, J. W., Westenbroek, R. E., Warner, C., Ahlijanian, M. K., Prystay, W., Gilbert, M. M., …
705 Catterall, W. A. (1993). Identification and differential subcellular localization of the neuronal
706 class C and class D L-type calcium channel alpha 1 subunits. *Journal of Cell Biology*,
707 *123*(4), 949–962. https://doi.org/10.1083/jcb.123.4.949
708 Hu, Z., Tong, X.-J., & Kaplan, J. M. (2013). UNC-13L, UNC-13S, and Tomosyn form a protein
709 code for fast and slow neurotransmitter release in Caenorhabditis elegans. *ELife*, *2*,
710 e00967. https://doi.org/10.7554/eLife.00967
711 Imig, C., Min, S.-W., Krinner, S., Arancillo, M., Rosenmund, C., Südhof, T. C., … Cooper, B. H.
712 (2014). The Morphological and Molecular Nature of Synaptic Vesicle Priming at
713 Presynaptic Active Zones. *Neuron*, *84*(2), 416–431.
714 https://doi.org/https://doi.org/10.1016/j.neuron.2014.10.009
715 J.G. White, E. Southgate, J.N. Thomson, & S. Brenner. (1986). The structure of the nervous
716 system of the nematode *Caenorhabditis elegans*. *Philosophical Transactions of the Royal*
717 *Society of London. B, Biological Sciences*, *314*(1165), 1–340.
718 https://doi.org/10.1098/rstb.1986.0056
719 Juette, M. F., Gould, T. J., Lessard, M. D., Mlodzianoski, M. J., Nagpure, B. S., Bennett, B. T.,
720 … Bewersdorf, J. (2008). Three-dimensional sub–100 nm resolution fluorescence
721 microscopy of thick samples. *Nature Methods*, *5*(6), 527–529.

https://doi.org/10.1038/nmeth.1211

Katz, E., Ferro, P. A., Weisz, G., & Uchitel, O. D. (1996). Calcium channels involved in synaptic transmission at the mature and regenerating mouse neuromuscular junction. *The Journal of Physiology*, *497*(3), 687–697. https://doi.org/10.1113/jphysiol.1996.sp021800

Kawabe, H., Mitkovski, M., Kaeser, P. S., Hirrlinger, J., Opazo, F., Nestvogel, D., … Brose, N. (2017). ELKS1 localizes the synaptic vesicle priming protein bMunc13-2 to a specific subset of active zones. *The Journal of Cell Biology*, *216*(4), 1143–1161. https://doi.org/10.1083/jcb.201606086

Krick, N., Ryglewski, S., Pichler, A., Bikbaev, A., Götz, T., Kobler, O., … Duch, C. (2021). Separation of presynaptic Ca_v2 and Ca_v1 channel function in synaptic vesicle exo- and endocytosis by the membrane anchored Ca²⁺ pump PMCA. *Proceedings of the National Academy of Sciences*, *118*(28), e2106621118. https://doi.org/10.1073/pnas.2106621118

Kurshan, P. T., Merrill, S. A., Dong, Y., Ding, C., Hammarlund, M., Bai, J., … Shen, K. (2018). γ-Neurexin and Frizzled Mediate Parallel Synapse Assembly Pathways Antagonized by Receptor Endocytosis. *Neuron*, *100*(1), 150-166.e4. https://doi.org/10.1016/j.neuron.2018.09.007

Kusick, G. F., Chin, M., Raychaudhuri, S., Lippmann, K., Adula, K. P., Hujber, E. J., … Watanabe, S. (2020). Synaptic vesicles transiently dock to refill release sites. *Nature Neuroscience*, *23*(11), 1329–1338. https://doi.org/10.1038/s41593-020-00716-1

Kwok, T. C. Y., Ricker, N., Fraser, R., Chan, A. W., Burns, A., Stanley, E. F., … Roy, P. J. (2006). A small-molecule screen in C. elegans yields a new calcium channel antagonist. *Nature*, *441*(7089), 91–95. https://doi.org/10.1038/nature04657

Lai, Y., Choi, U. B., Leitz, J., Rhee, H. J., Lee, C., Altas, B., … Brunger, A. T. (2017). Molecular Mechanisms of Synaptic Vesicle Priming by Munc13 and Munc18. *Neuron*, *95*(3), 591-607.e10. https://doi.org/https://doi.org/10.1016/j.neuron.2017.07.004

Lainé, V., Ségor, J. R., Zhan, H., Bessereau, J.-L., & Jospin, M. (2014). Hyperactivation of L-type voltage-gated Ca2+ channels in Caenorhabditis elegans striated muscle can result from point mutations in the IS6 or the IIIS4 segment of the α1 subunit. *Journal of Experimental Biology*, *217*(21), 3805–3814. https://doi.org/10.1242/jeb.106732

Lee, R. Y., Lobel, L., Hengartner, M., Horvitz, H. R., & Avery, L. (1997). Mutations in the alpha1 subunit of an L-type voltage-activated Ca2+ channel cause myotonia in Caenorhabditis elegans. *The EMBO Journal*, *16*(20), 6066–6076. https://doi.org/10.1093/emboj/16.20.6066

Liu, H., Li, L., Nedelcu, D., Hall, Q., Zhou, L., Wang, W., … Hu, Z. (2019). Heterodimerization of UNC-13/RIM regulates synaptic vesicle release probability but not priming in C. elegans. *ELife*, *8*, e40585. https://doi.org/10.7554/eLife.40585

Liu, H., Li, L., Wang, W., Gong, J., Yang, X., & Hu, Z. (2018). Spontaneous Vesicle Fusion Is Differentially Regulated at Cholinergic and GABAergic Synapses. *Cell Reports*, *22*(9), 2334–2345. https://doi.org/https://doi.org/10.1016/j.celrep.2018.02.023

Liu, P., Ge, Q., Chen, B., Salkoff, L., Kotlikoff, M. I., & Wang, Z.-W. (2011). Genetic dissection of ion currents underlying all-or-none action potentials in C. elegans body-wall muscle cells. *The Journal of Physiology*, *589*(1), 101–117. https://doi.org/10.1113/jphysiol.2010.200683

Liu, Ping, Chen, B., Mailler, R., & Wang, Z.-W. (2017). Antidromic-rectifying gap junctions amplify chemical transmission at functionally mixed electrical-chemical synapses. *Nature Communications*, *8*(1), 14818. https://doi.org/10.1038/ncomms14818

Liu, Ping, Chen, B., & Wang, Z.-W. (2014). SLO-2 potassium channel is an important regulator of neurotransmitter release in Caenorhabditis elegans. *Nature Communications*, *5*(1), 5155. https://doi.org/10.1038/ncomms6155

Liu, Q. (2005). Presynaptic Ryanodine Receptors Are Required for Normal Quantal Size at the Caenorhabditis elegans Neuromuscular Junction. *Journal of Neuroscience*, *25*(29), 6745–6754. https://doi.org/10.1523/JNEUROSCI.1730-05.2005

Liu, Qiang, Chen, B., Yankova, M., Morest, D. K., Maryon, E., Hand, A. R., … Wang, Z.-W. (2005). Presynaptic ryanodine receptors are required for normal quantal size at the

Caenorhabditis elegans neuromuscular junction. *The Journal of Neuroscience : The Official Journal of the Society for Neuroscience*, *25*(29), 6745–6754. https://doi.org/10.1523/JNEUROSCI.1730-05.2005

Liu, Qiang, Hollopeter, G., & Jorgensen, E. M. (2009). Graded synaptic transmission at the Caenorhabditis elegans neuromuscular junction. *Proceedings of the National Academy of Sciences*, *106*(26), 10823. https://doi.org/10.1073/pnas.0903570106

Liu, Qiang, Kidd, P. B., Dobosiewicz, M., & Bargmann, C. I. (2018). C. elegans AWA Olfactory Neurons Fire Calcium-Mediated All-or-None Action Potentials. *Cell*, *175*(1), 57-70.e17. https://doi.org/https://doi.org/10.1016/j.cell.2018.08.018

Lu, J., Machius, M., Dulubova, I., Dai, H., Südhof, T. C., Tomchick, D. R., & Rizo, J. (2006). Structural Basis for a Munc13–1 Homodimer to Munc13–1/RIM Heterodimer Switch. *PLOS Biology*, *4*(7), e192-. Retrieved from https://doi.org/10.1371/journal.pbio.0040192

Maduro, M., & Pilgrim, D. (1995). Identification and cloning of unc-119, a gene expressed in the Caenorhabditis elegans nervous system. *Genetics*, *141*(3), 977–988. https://doi.org/10.1093/genetics/141.3.977

Marques, F., Thapliyal, S., Javer, A., Shrestha, P., Brown, A. E. X., & Glauser, D. A. (2020). Tissue-specific isoforms of the single C. elegans Ryanodine receptor gene unc-68 control specific functions. *PLOS Genetics*, *16*(10), e1009102. https://doi.org/10.1371/journal.pgen.1009102

McRory, J. E., Hamid, J., Doering, C. J., Garcia, E., Parker, R., Hamming, K., … Snutch, T. P. (2004). The CACNA1F Gene Encodes an L-Type Calcium Channel with Unique Biophysical Properties and Tissue Distribution. *The Journal of Neuroscience*, *24*(7), 1707. https://doi.org/10.1523/JNEUROSCI.4846-03.2004

Mlodzianoski, M. J., Juette, M. F., Beane, G. L., & Bewersdorf, J. (2009). Experimental characterization of 3D localization techniques for particle-tracking and super-resolution microscopy. *Opt. Express*, *17*(10), 8264–8277. https://doi.org/10.1364/OE.17.008264

Mollwitz, B., Brunk, E., Schmitt, S., Pojer, F., Bannwarth, M., Schiltz, M., … Johnsson, K. (2012). Directed Evolution of the Suicide Protein *O* ^{6} -Alkylguanine-DNA Alkyltransferase for Increased Reactivity Results in an Alkylated Protein with Exceptional Stability. *Biochemistry*, *51*(5), 986–994. https://doi.org/10.1021/bi2016537

Nakamura, Y., Harada, H., Kamasawa, N., Matsui, K., Rothman, J. S., Shigemoto, R., … Takahashi, T. (2015). Nanoscale Distribution of Presynaptic Ca2+ Channels and Its Impact on Vesicular Release during Development. *Neuron*, *85*(1), 145–158. https://doi.org/https://doi.org/10.1016/j.neuron.2014.11.019

Nanou, E., & Catterall, W. A. (2018). Calcium Channels, Synaptic Plasticity, and Neuropsychiatric Disease. *Neuron*, *98*(3), 466–481. https://doi.org/https://doi.org/10.1016/j.neuron.2018.03.017

Naranjo, D., Wen, H., & Brehm, P. (2015). Zebrafish CaV2.1 Calcium Channels Are Tailored for Fast Synchronous Neuromuscular Transmission. *Biophysical Journal*, *108*(3), 578–584. https://doi.org/https://doi.org/10.1016/j.bpj.2014.11.3484

Neher, E., & Brose, N. (2018). Dynamically Primed Synaptic Vesicle States: Key to Understand Synaptic Short-Term Plasticity. *Neuron*, *100*(6), 1283–1291. https://doi.org/https://doi.org/10.1016/j.neuron.2018.11.024

Özçete, Ö. D., & Moser, T. (2021). A sensory cell diversifies its output by varying Ca2+ influx-release coupling among active zones. *The EMBO Journal*, *40*(5), e106010. https://doi.org/https://doi.org/10.15252/embj.2020106010

Piggott, C. A., & Jin, Y. (2021). Junctophilins: Key Membrane Tethers in Muscles and Neurons. *Frontiers in Molecular Neuroscience*, *14*, 141. Retrieved from https://www.frontiersin.org/article/10.3389/fnmol.2021.709390

Platzer, J., Engel, J., Schrott-Fischer, A., Stephan, K., Bova, S., Chen, H., … Striessnig, J. (2000). Congenital Deafness and Sinoatrial Node Dysfunction in Mice Lacking Class D L-Type Ca2+ Channels. *Cell*, *102*(1), 89–97. https://doi.org/https://doi.org/10.1016/S0092-8674(00)00013-1

828 Pokala, N., Liu, Q., Gordus, A., & Bargmann, C. I. (2014). Inducible and titratable silencing of
829 Caenorhabditis elegans neurons in vivo with histamine-gated chloride channels.
830 *Proceedings of the National Academy of Sciences*, *111*(7), 2770–2775.
831 https://doi.org/10.1073/pnas.1400615111
832 Pym, E., Sasidharan, N., Thompson-Peer, K. L., Simon, D. J., Anselmo, A., Sadreyev, R., …
833 Kaplan, J. M. (2017). Shank is a dose-dependent regulator of Cav1 calcium current and
834 CREB target expression. *ELife*, *6*, e18931. https://doi.org/10.7554/eLife.18931
835 Quade, B., Camacho, M., Zhao, X., Orlando, M., Trimbuch, T., Xu, J., … Rizo, J. (2019).
836 Membrane bridging by Munc13-1 is crucial for neurotransmitter release. *ELife*, *8*, e42806.
837 https://doi.org/10.7554/eLife.42806
838 Rebola, N., Reva, M., Kirizs, T., Szoboszlay, M., Lőrincz, A., Moneron, G., … DiGregorio, D. A.
839 (2019). Distinct Nanoscale Calcium Channel and Synaptic Vesicle Topographies
840 Contribute to the Diversity of Synaptic Function. *Neuron*, *104*(4), 693-710.e9.
841 https://doi.org/https://doi.org/10.1016/j.neuron.2019.08.014
842 Rey, S., Maton, G., Satake, S., Llano, I., Kang, S., Surmeier, D. J., … Collin, T. (2020).
843 Physiological involvement of presynaptic L-type voltage-dependent calcium channels in
844 GABA release of cerebellar molecular layer interneurons. *Journal of Neurochemistry*,
845 *155*(4), 390–402. https://doi.org/10.1111/jnc.15100
846 Richmond, J E, Weimer, R. M., & Jorgensen, E. M. (2001). An open form of syntaxin bypasses
847 the requirement for UNC-13 in vesicle priming. *Nature*, *412*(6844), 338–341.
848 https://doi.org/10.1038/35085583
849 Richmond, Janet E, Davis, W. S., & Jorgensen, E. M. (1999). UNC-13 is required for synaptic
850 vesicle fusion in C. elegans. *Nature Neuroscience*, *2*(11), 959–964.
851 https://doi.org/10.1038/14755
852 Sahu, G., Wazen, R.-M., Colarusso, P., Chen, S. R. W., Zamponi, G. W., & Turner, R. W.
853 (2019). Junctophilin Proteins Tether a Cav1-RyR2-KCa3.1 Tripartite Complex to Regulate
854 Neuronal Excitability. *Cell Reports*, *28*(9), 2427-2442.e6.
855 https://doi.org/https://doi.org/10.1016/j.celrep.2019.07.075
856 Schmitz, Y., & Witkovsky, P. (1997). Dependence of photoreceptor glutamate release on a
857 dihydropyridine-sensitive calcium channel. *Neuroscience*, *78*(4), 1209–1216.
858 https://doi.org/https://doi.org/10.1016/S0306-4522(96)00678-1
859 Schneggenburger, R., & Neher, E. (2000). Intracellular calcium dependence of transmitter
860 release rates at a fast central synapse. *Nature*, *406*(6798), 889–893.
861 https://doi.org/10.1038/35022702
862 Schneider, M. F. (1994). Control of Calcium Release in Functioning Skeletal Muscle Fibers.
863 *Annual Review of Physiology*, *56*(1), 463–484.
864 https://doi.org/10.1146/annurev.ph.56.030194.002335
865 Schwartz, M. L., & Jorgensen, E. M. (2016). SapTrap, a Toolkit for High-Throughput
866 CRISPR/Cas9 Gene Modification in Caenorhabditis elegans. *Genetics*, *202*(4), 1277–1288.
867 https://doi.org/10.1534/genetics.115.184275
868 Siksou, L., Varoqueaux, F., Pascual, O., Triller, A., Brose, N., & Marty, S. (2009). A common
869 molecular basis for membrane docking and functional priming of synaptic vesicles.
870 *European Journal of Neuroscience*, *30*(1), 49–56.
871 https://doi.org/https://doi.org/10.1111/j.1460-9568.2009.06811.x
872 Südhof, T. C. (2012). The Presynaptic Active Zone. *Neuron*, *75*(1), 11–25.
873 https://doi.org/https://doi.org/10.1016/j.neuron.2012.06.012
874 Tong, X.-J., López-Soto, E. J., Li, L., Liu, H., Nedelcu, D., Lipscombe, D., … Kaplan, J. M.
875 (2017). Retrograde Synaptic Inhibition Is Mediated by α-Neurexin Binding to the α2δ
876 Subunits of N-Type Calcium Channels. *Neuron*, *95*(2), 326-340.e5.
877 https://doi.org/https://doi.org/10.1016/j.neuron.2017.06.018
878 Topalidou, I., Cattin-Ortolá, J., Pappas, A. L., Cooper, K., Merrihew, G. E., MacCoss, M. J., &
879 Ailion, M. (2016). The EARP Complex and Its Interactor EIPR-1 Are Required for Cargo
880 Sorting to Dense-Core Vesicles. *PLOS Genetics*, *12*(5), e1006074.

https://doi.org/10.1371/journal.pgen.1006074

Tsien, R W, Lipscombe, D., Madison, D. v, Bley, K. R., & Fox, A. P. (1988). Multiple types of neuronal calcium channels and their selective modulation. *Trends in Neurosciences*, *11*(10), 431–438. https://doi.org/https://doi.org/10.1016/0166-2236(88)90194-4

Tsien, Richard W, & Tsien, R. Y. (1990). Calcium channels, stores, and oscillations. *Annual Review of Cell Biology*, *6*(1), 715–760.

Urbano, F. J., & Uchitel, O. D. (1999). L-Type calcium channels unmasked by cell-permeant Ca 2+ buffer at mouse motor nerve terminals. *Pfl*[illegible]*gers Archiv European Journal of Physiology*, *437*(4), 523–528. https://doi.org/10.1007/s004240050813

Vyleta, N. P., & Jonas, P. (2014). Loose Coupling Between Ca $^{2+}$ Channels and Release Sensors at a Plastic Hippocampal Synapse. *Science*, *343*(6171), 665–670. https://doi.org/10.1126/science.1244811

Watanabe, S., Davis, M. W., Kusick, G. F., Iwasa, J., & Jorgensen, E. M. (2020). SynapsEM: Computer-Assisted Synapse Morphometry. *Frontiers in Synaptic Neuroscience*, *12*. Retrieved from https://www.frontiersin.org/article/10.3389/fnsyn.2020.584549

Watanabe, S., Liu, Q., Davis, M. W., Hollopeter, G., Thomas, N., Jorgensen, N. B., & Jorgensen, E. M. (2013). Ultrafast endocytosis at Caenorhabditis elegans neuromuscular junctions. *ELife*, *2*, e00723. https://doi.org/10.7554/eLife.00723

Weber, A. M., Wong, F. K., Tufford, A. R., Schlichter, L. C., Matveev, V., & Stanley, E. F. (2010). N-type Ca2+ channels carry the largest current: implications for nanodomains and transmitter release. *Nature Neuroscience*, *13*(11), 1348–1350. https://doi.org/10.1038/nn.2657

Weimer, R. M., Gracheva, E. O., Meyrignac, O., Miller, K. G., Richmond, J. E., & Bessereau, J.-L. (2006). UNC-13 and UNC-10/Rim Localize Synaptic Vesicles to Specific Membrane Domains. *The Journal of Neuroscience*, *26*(31), 8040. https://doi.org/10.1523/JNEUROSCI.2350-06.2006

Yang, X., Wang, S., Sheng, Y., Zhang, M., Zou, W., Wu, L., … Ma, C. (2015). Syntaxin opening by the MUN domain underlies the function of Munc13 in synaptic-vesicle priming. *Nature Structural & Molecular Biology*, *22*(7), 547–554. https://doi.org/10.1038/nsmb.3038

Yu, H., Yuan, C., Westenbroek, R. E., & Catterall, W. A. (2018). The AKAP Cypher/Zasp contributes to β-adrenergic/PKA stimulation of cardiac CaV1.2 calcium channels. *Journal of General Physiology*, *150*(6), 883–889. https://doi.org/10.1085/jgp.201711818

Zhang, S. Y., Robertson, D., Yates, G., & Everett, A. (1999). Role of L-Type Ca $^{2+}$ Channels in Transmitter Release From Mammalian Inner Hair Cells I. Gross Sound-Evoked Potentials. *Journal of Neurophysiology*, *82*(6), 3307–3315. https://doi.org/10.1152/jn.1999.82.6.3307

Zhang, X., Chen, X., Zeng, Z., Zhang, M., Sun, Y., Xi, P., … Xu, P. (2015). Development of a reversibly switchable fluorescent protein for super-resolution optical fluctuation imaging (SOFI). *ACS Nano*, *9*(3), 2659–2667. https://doi.org/10.1021/nn5064387

Zhou, K., Stawicki, T. M., Goncharov, A., & Jin, Y. (2013). Position of UNC-13 in the active zone regulates synaptic vesicle release probability and release kinetics. *ELife*, *2*, e01180. https://doi.org/10.7554/eLife.01180

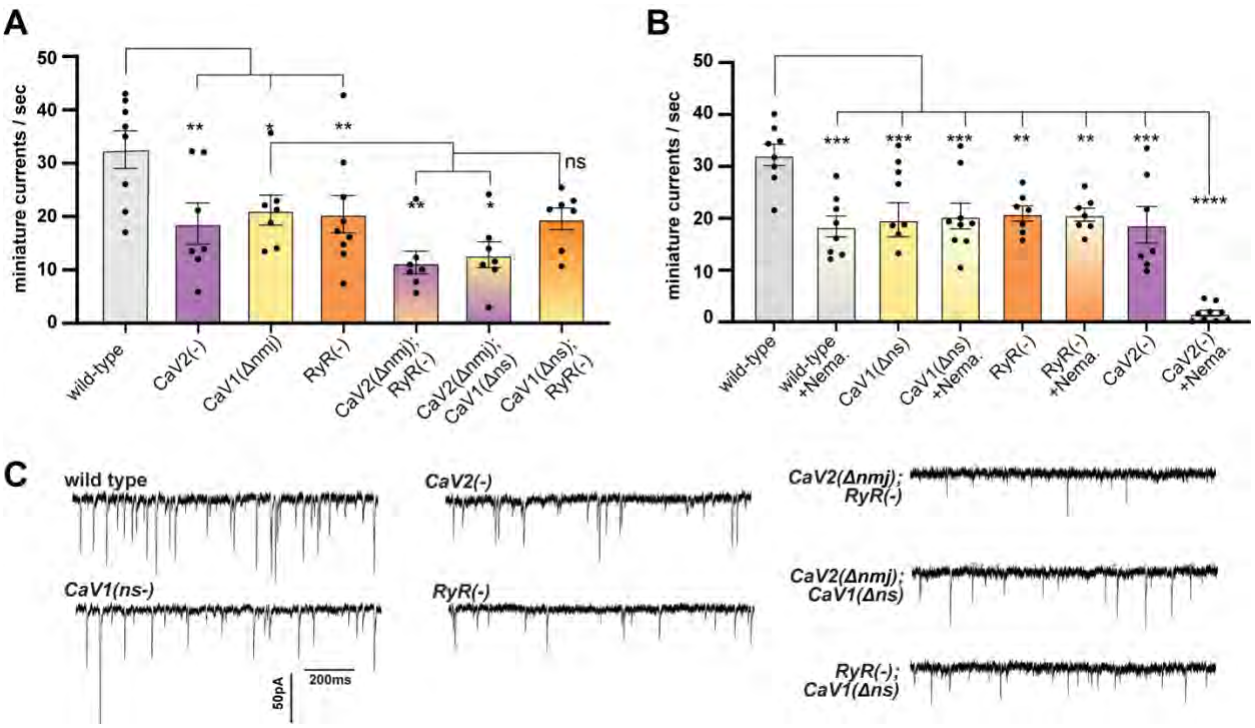

Figure 1. CaV2 and CaV1-RyR release acetylcholine vesicles at the *C. elegans* neuromuscular junction.

(a) CaV2 and CaV1-RyR additive contributions to spontaneous release. At 0.5mM calcium, N2 wild-type 33 ± 4 minis/s n=8, and single mutants *unc-2(lj1)* 19 ± 4 minis/s n=7 (*p<0.05 versus N2), *egl-19(st556)*;*oxTi1047* (EG9034) are CaV1 null animals with a single copy transgene insertion rescuing egl-19 in muscle, but not in neurons, will be referred to as CaV1(Δns) for brevity, 21 ± 3 minis/s n=7, *unc-68(e540)* (CB540) 20 ± 4 minis/s n=9. CaV2(Δcord) double mutants: *unc-2(lj1);unc-68(e540)*;oxEx2097 (EG9405) 11 ± 2 minis/s n=7, *unc-2(lj1);egl-19(st556);oxTi1047*; oxEx2097 (EG9406) 13 ± 2 minis/s n=7, and viable double mutant *egl-19(st556);oxTi1047;unc-68(e540)* (EG8827) 20 ± 2 minis/s n=7.

(b) Spontaneous neurotransmission by CaV1 and RyR are inhibited by nemadipine. At 0.5mM calcium, N2 wild-type 32 ± 2 minis/s n=8, with nemadipine 18 ± 2 mini/s n=8. *egl-19(st556);oxTi1047* (EG9034) 20 ± 3 minis/s n=10, with nemadipine 20 ± 2 mini/s n=9. *unc-68(e540)* (CB540) 21 ± 1 minis/s n=7, with nemadipine 21 ± 1 mini/s n=7. Single mutants *unc-2(lj1)* 19 ± 4 minis/s n=7, with nemadipine 2 ± 1 mini/s n=9.

(c) Sample traces of spontaneous release in 0.5mM extracellular calcium. Error reported in SEM. *p<0.05 **p<0.005 by Welch's t-test.

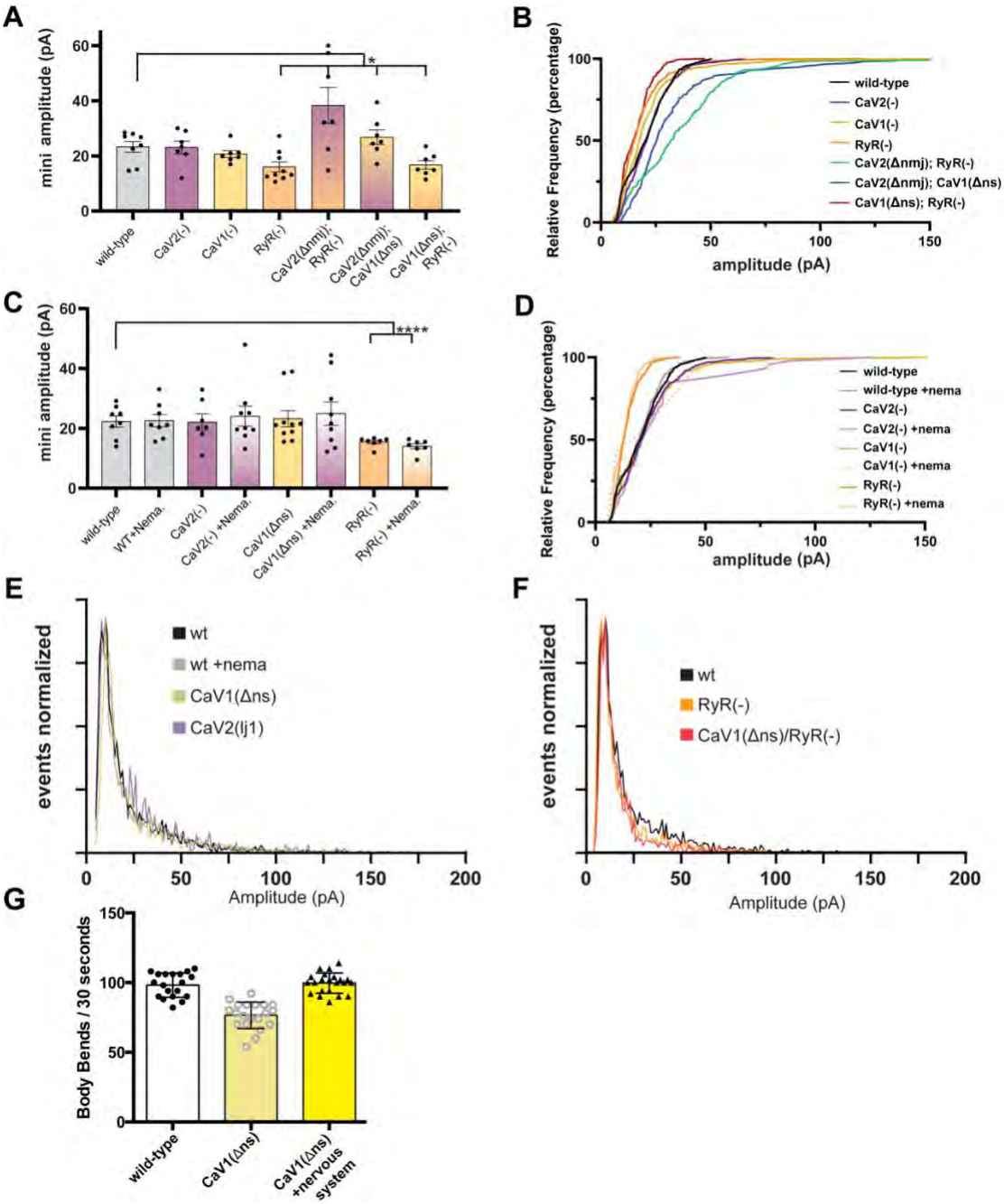

Extended Data Figure 1. Calcium channel miniature amplitudes.

(a) RyR is required for large-amplitude spontaneous events. At 0.5mM calcium, N2 wild-type 23 ± 2 pA n=8, and single mutants *unc-2(lj1)* 23 ± 2 pA n=7, *egl-19(st556);oxTi1047* (EG9034) 21 ± 1 pA n=7*, unc-68(e540)* (CB540) 16 ± 2 pA n=9. CaV2(Δcord) double *mutants unc-2(lj1);unc-68(e540);* oxEx2097 (EG9405) 38 ± 3 pA n=7, *unc-2(lj1);egl-19(st556);oxTi1047;oxEx2097* (EG9406) 26 ± 3 pA n=7, and viable double mutant *egl-19(st556);oxTi1047;unc-68(e540)* (EG8827) 17 ± 2 pA n=7.
(b) Cumulative distribution plot of mutant amplitudes
(c) Nemadipine does not inhibit large-amplitude spontaneous events. At 0.5mM calcium, N2 wild-type 22 ± 2 pA n=8, with nemadipine 23 ± 2 pA n=8. Single mutants *unc-2(lj1)* 22 ± 3 pA n=7, with nemadipine 24 ± 3 pA n=9. *egl-19(st556);oxTi1047* (EG9034) 23 ± 3 pA n=10, with nemadipine 25 ± 4 pA n=9. *unc-68(e540)* (CB540) 15 ± 1 pA n=7, with nemadipine 14 ± 1 pA n=7.
(d) Cumulative distribution plot of nemadipine treatment amplitudes.
(e) Frequency distribution plot of calcium mutant amplitudes normalized to the mode.
(f) Frequency distribution plot of ryanodine mutants with reduced amplitudes, normalized to mode.

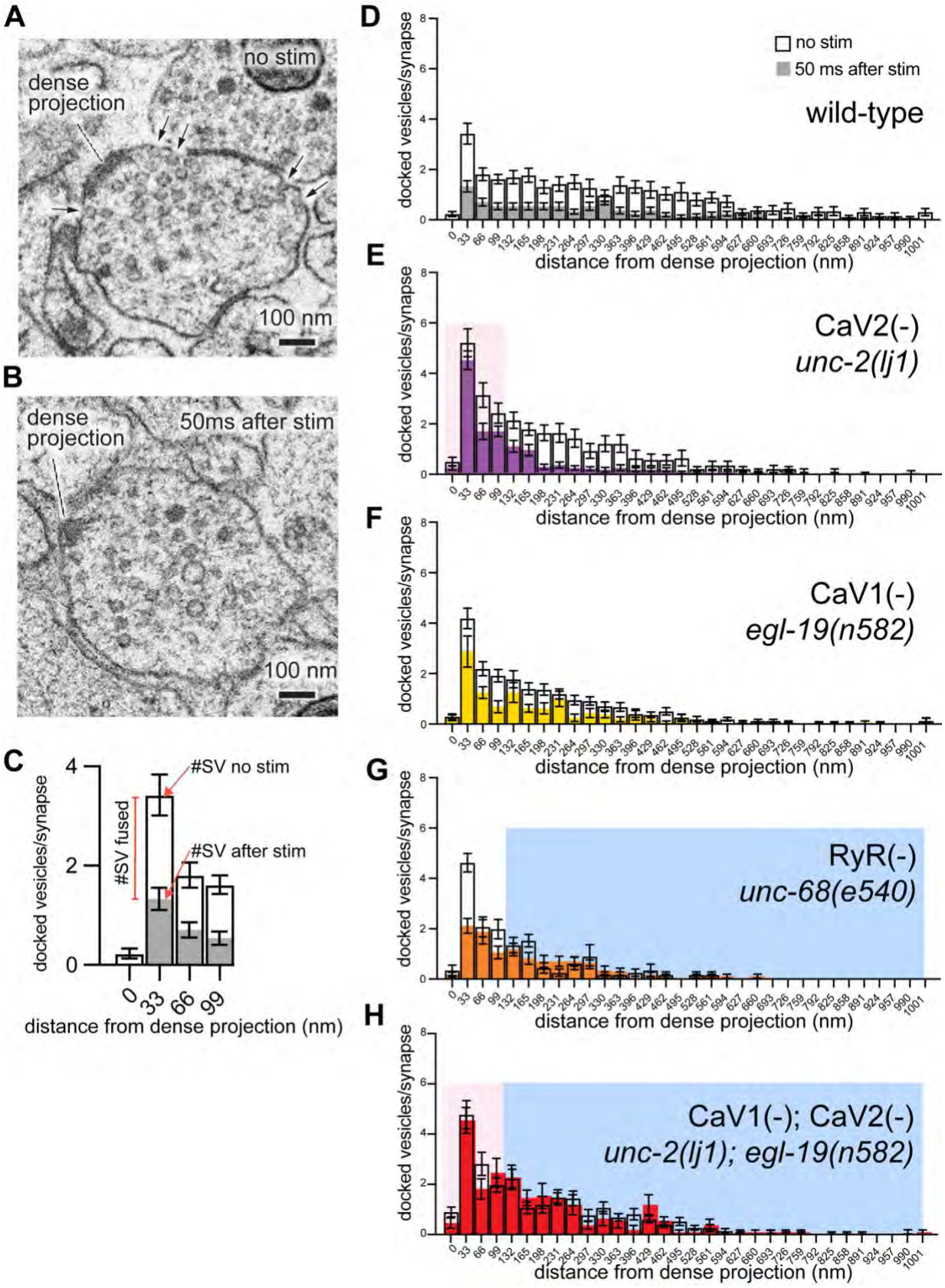

Figure 2. CaV2 and CaV1-RyR act at distinct vesicle release sites.
(a-b) Docked vesicles (black arrows) are present near dense projections in electron micrograph of unstimulated animals, but not 50ms after stimulation by channelrhodopsin.

(c) cartoon diagram of interpretation of fusion histograms. The number of synaptic vesicles fused by stimulation can be determined by comparing the number of synaptic vesicles docked at the active zone at a given distance range before and after stimulation.
(d-h) Average number of docked vesicles per synapse in animals with and without stimulation by channelrhodopsin.
(d) Wild-type animals contain fewer docked vesicles at all locations after stimulation.
(g) CaV2 mutant *unc-2(lj1)* retains docked vesicles within 100nm of dense projections after stimulation.
(f) CaV1 mutant *egl-19(n582)* has vesicle fusion defects at all distances.
(g) Docked vesicles within 100nm of dense projections are reduced in RyR mutant *unc-68(e540*) while retaining lateral vesicles.
(h) Double mutant disrupting CaV1 *egl-19(n582)* and CaV2 *unc-2(lj1)* exhibit no change in docked vesicles after stimulation N=2 animals. N2(nostim), n=26 synapses. N2(stim) n = 24 synapses. CaV2(nostim) n=14. CaV2(stim) n=27 synapses. CaV1(nostim) n=29 synapses. CaV1(stim) n=16 synapses. RyR(nostim) n=11 synapses. RyR(stim) n=17 synapses. CaV2;CaV1(nostim) n=24 synapses. CaV2;CaV1(stim) n=17 synapses. Errors given in SEM.

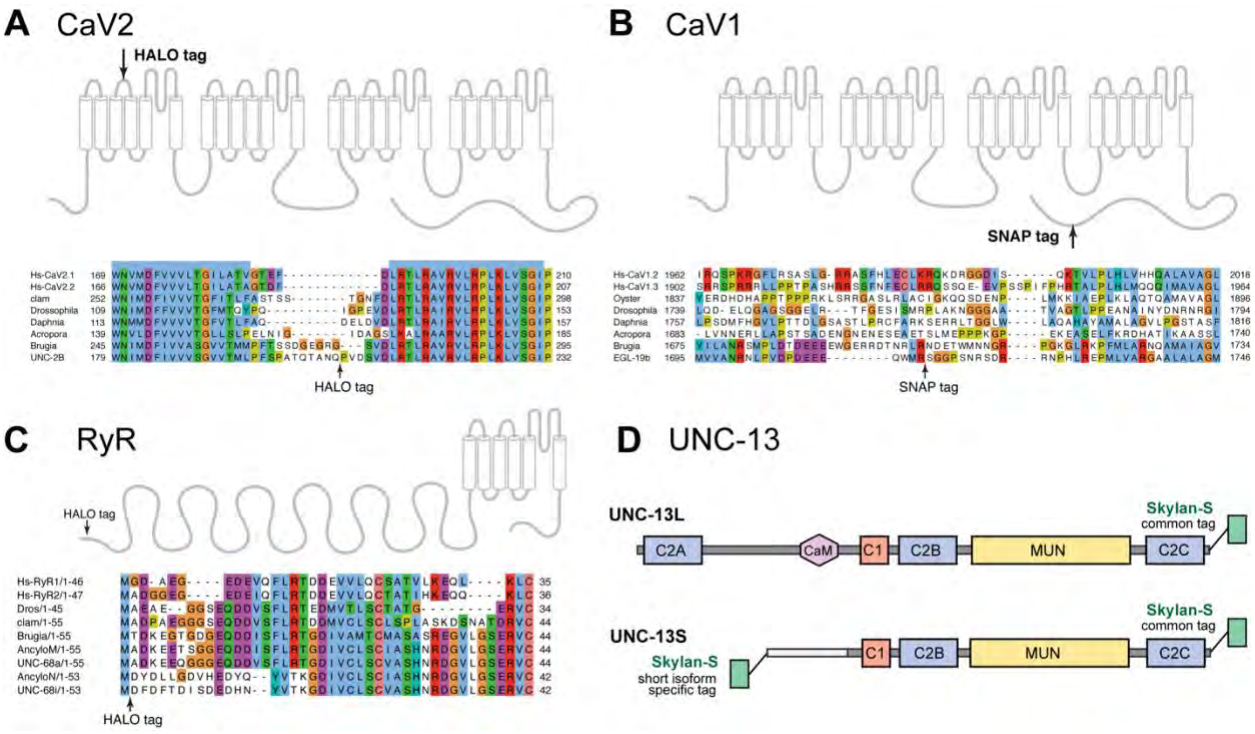

Extended Data Figure 2. Calcium channel and UNC-13 tagging strategy.
(a-c), Tagging strategies and sites used for CRISPR/Cas9 tagging of the endogenous loci of CaV2, CaV1, and RyR.

(d) tagging strategy at the endogenous locus of *unc-13* CRISPR/Cas9. C-terminal tag labels all isoforms of UNC-13. N-termini are unique to the long and short isoform, thus short can be exclusively tagged.

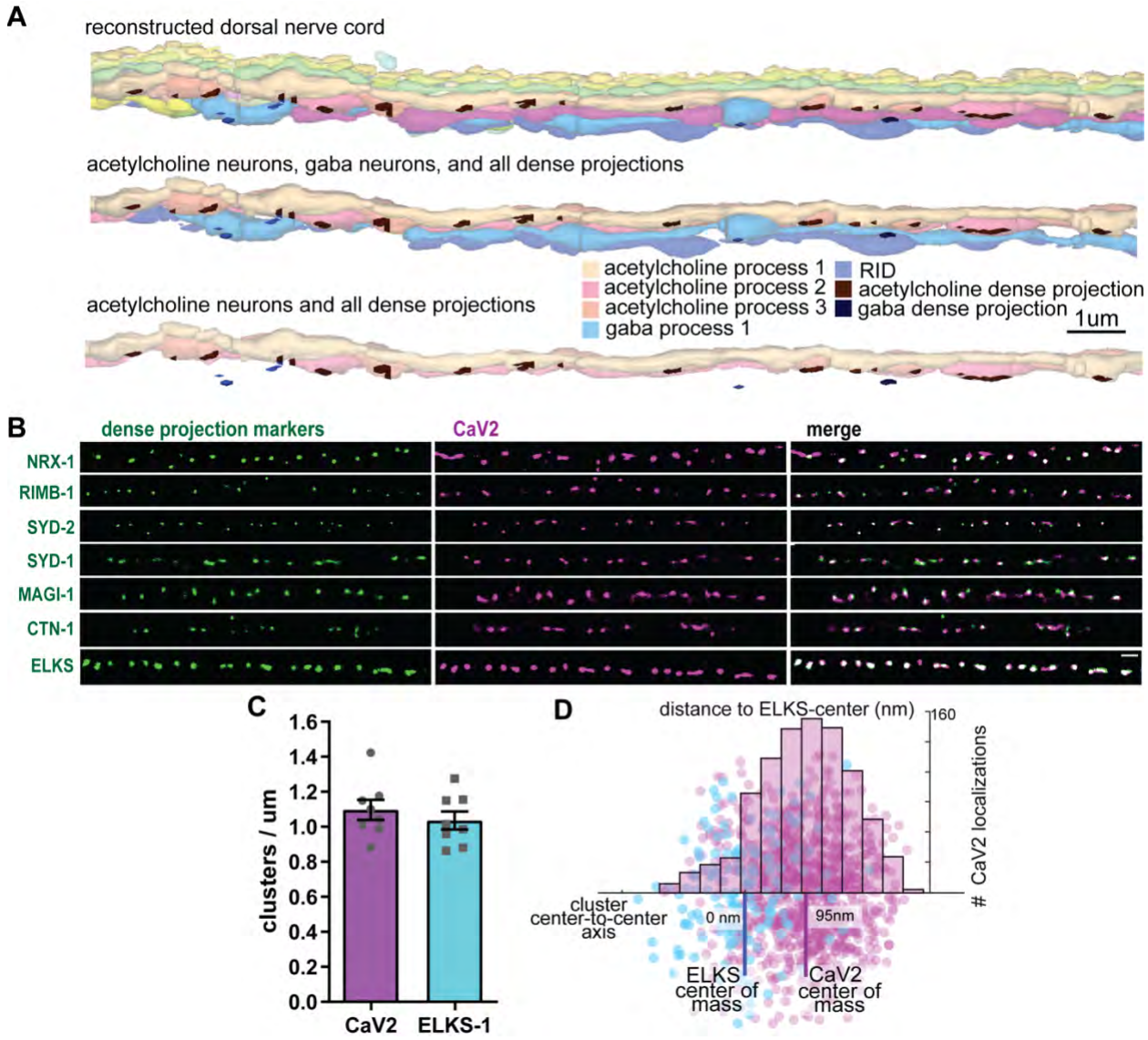

Figure 3. Dorsal nerve cord reconstruction and candidate dense projection markers.
(a) 20-micron reconstruction of N2 *C. elegans* dorsal nerve cord from 100nm sections. Image was oriented to reproduce the positioning used for all SML microscopy in this study. Scale bar 1um.
(b) CaV2 colocalizes with a number of cytomatrix active zone proteins. Super-resolution images of various Skylan-S tagged cytomatrix active zone proteins versus CaV2::HALO.
(c) Clusters of ELKS and CaV2 per micron of dorsal nerve cord from super-resolution image analysis.
(d) Localization plot tool (Proberuler) example diagram of a single ELKS(cyan) and CaV2(magenta) synapse. Cluster centers are marked by solid lines.

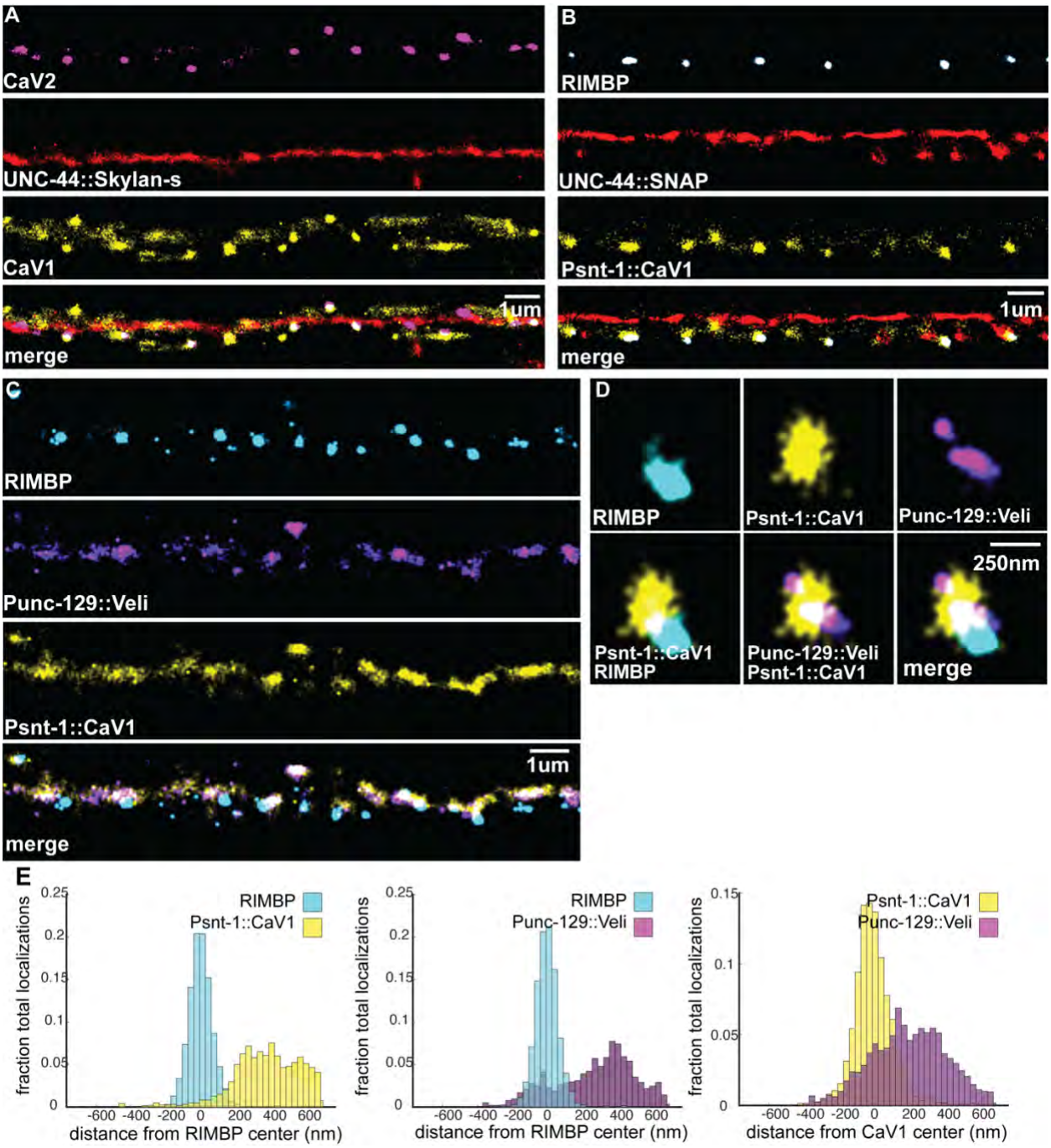

Extended Data Figure 3. Neuronal CaV1 forms clusters at presynaptic boutons.
Comparison of endogenously tagged CaV1 and exogenously rescued Psnt-1::CaV1.
(a) endogenous CaV1. Localization microscopy images of dorsal nerve cord with CaV2/*unc-2[(ox672)HALO*]::HTL-JF646 (purple), and CaV1/*egl-19[(ox728)SNAP]::*STL-JF549cp (yellow) and Ankyrin/*unc-44[(ox802)SKY-S]* (red). scale bar = 1um.
(b) Exogenous CaV1. Localization microscopy images of dorsal nerve cord. In the *egl-19(st556)* background, CaV1 was rescued in muscle using a single copy transgene insertion of (*oxTi1047[Pset-18::egl-19b]*). CaV1 was rescued in neurons using a single copy transgene insertion of (*oxTi1055[Psnt-1::HALO::egl-19b]*). Labelled with *Psnt-1::CaV1/egl-19*(*oxTi1055[Psnt-1::HALO::egl-19*b])::HTL-JF646 (purple), *unc-44*::TMRStar (red) and RIMBP/*rimb-1[(ox704)SKY-S]* (cyan). scale bar = 1um.
(c) Neuronal CaV1 partially colocalizes with acetylcholine neuron driven Veli/LIN-7. Localization

microscopy images of dorsal nerve cord. Dense projections are marked by RIMBP/*rimb-1(ox704[SKY-S])*. In the *egl-19(st556)* background, CaV1 was rescued in muscle using a single copy transgene insertion of *(oxTi1047[Pset-18::egl-19b])*. CaV1 was rescued in neurons using a single copy transgene insertion of *(oxTi1055[Psnt-1::HALO::egl-19b])*. Veli/*lin-7(oxEx2223[Punc-129::lin-7::SNAP]*) was expressed using the *unc-129* promotor as an extrachromosomal array. scale bar = 1um.

(d) Single synapse analysis of animals stained with HTL-JF646 (magenta) and STL-JF549cp (yellow). dense projections are marked by RIMBP/*rimb-1(ox704[SKY-S])* tagged with SKYLAN-S. In the *egl-19(st556)* background, CaV1 was rescued in muscle using a single copy transgene insertion of *(oxTi1047[Pset-18::egl-19b])*. CaV1 was rescued in neurons using a single copy transgene insertion of (oxTi1055[*Psnt-1::HALO::egl-19b*]). Veli/*LIN-7*(oxEx2223[*Punc-129::lin-7::SNAP*]) was overexpressed using the *unc-129* promotor as an extrachromosomal array. Scale bar = 250nm.

(e-g) Cumulative distribution plot of Psnt-1::CaV1(*oxTi1055[Psnt-1::HALO::egl-19b*]) to RIMBP/*rimb-1(ox704[SKY-S])* center and Veli/*lin-7(oxEx2223[Punc-129::lin-7::SNAP]) to* RIMBP/*rimb-1(ox704[SKY-S])* center measured from single synapses. n=24 synapses, N=5 animals

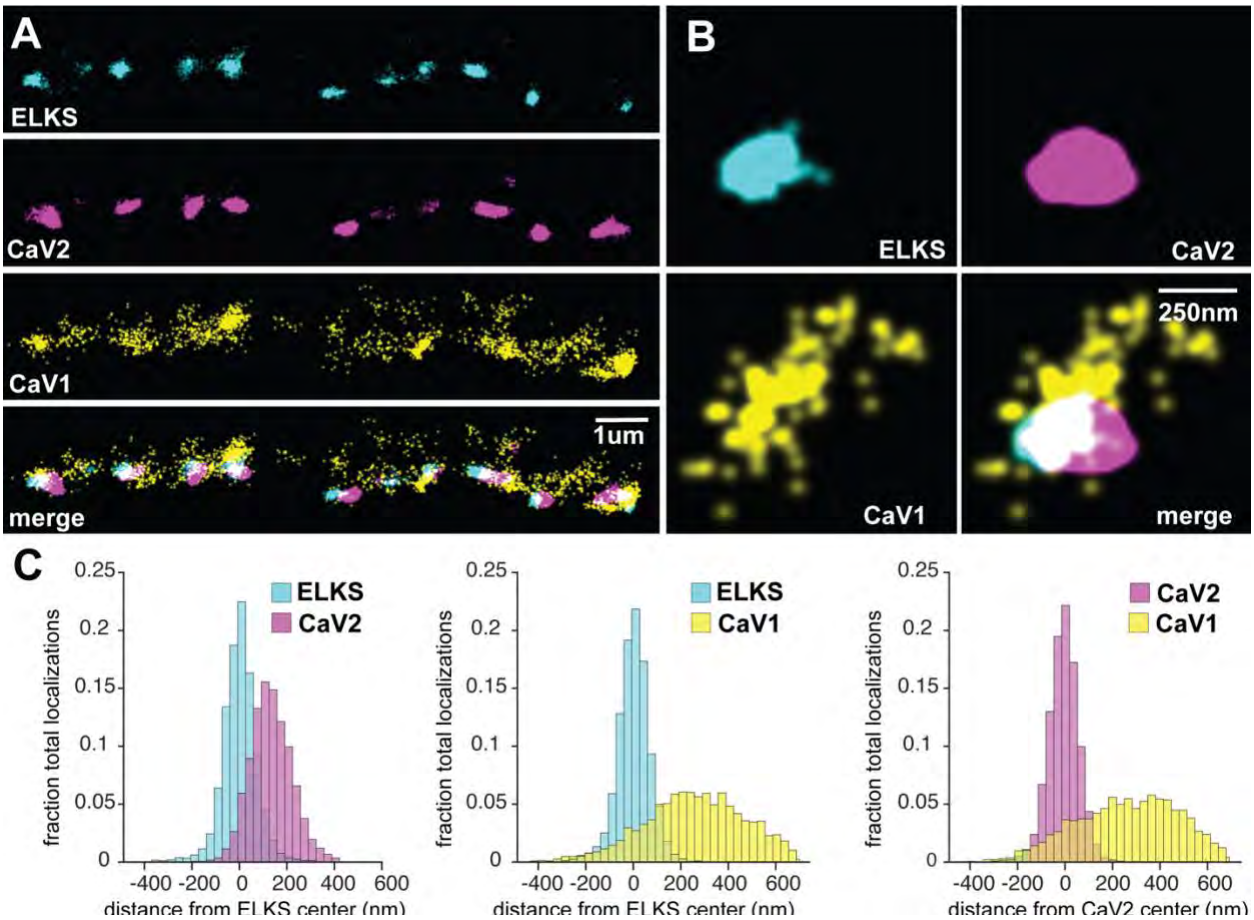

Figure 4. CaV2, CaV1, and ELKS localizations.

ELKS and CaV2 colocalize, CaV1 is diffuse and lateral to CaV2.

(a) Localization microscopy images of animals stained with HTL-JF646 (magenta) and STL-JF549pa (yellow). Dorsal cord images: active zones labeled by ELKS/*elks-1(ox747[SKY-S])* colocalize with CaV2/*unc-2(ox672[HALO])* but not CaV1/*egl-19(ox728[SNAP])*. Scale bar = 1um.

(b) Single synapse region of interests: active zones labeled by ELKS/*elks-1(ox747[SKY-S])* colocalize with CaV2/*unc-2(ox672[HALO])* but not CaV1/*egl-19(ox728[SNAP])*. Scale bar = 250nm

(c) Cumulative frequency distribution plot of distances from CaV2 localization to ELKS/*elks-1(ox747[SKY-S])* cluster center measured from single synapses. Cumulative frequency distribution plot of distances from CaV1/*egl-19(ox728[SNAP])* localization to ELKS/*elks-1(ox747[SKY-S])* cluster center measured from individual synapses.

Cumulative frequency distribution plot of distances from CaV1/*egl-19(ox728[SNAP])* localizations to CaV2/*unc-2(ox672[HALO])* cluster center measured from individual synapses. n=26 synapses, N=5 animals

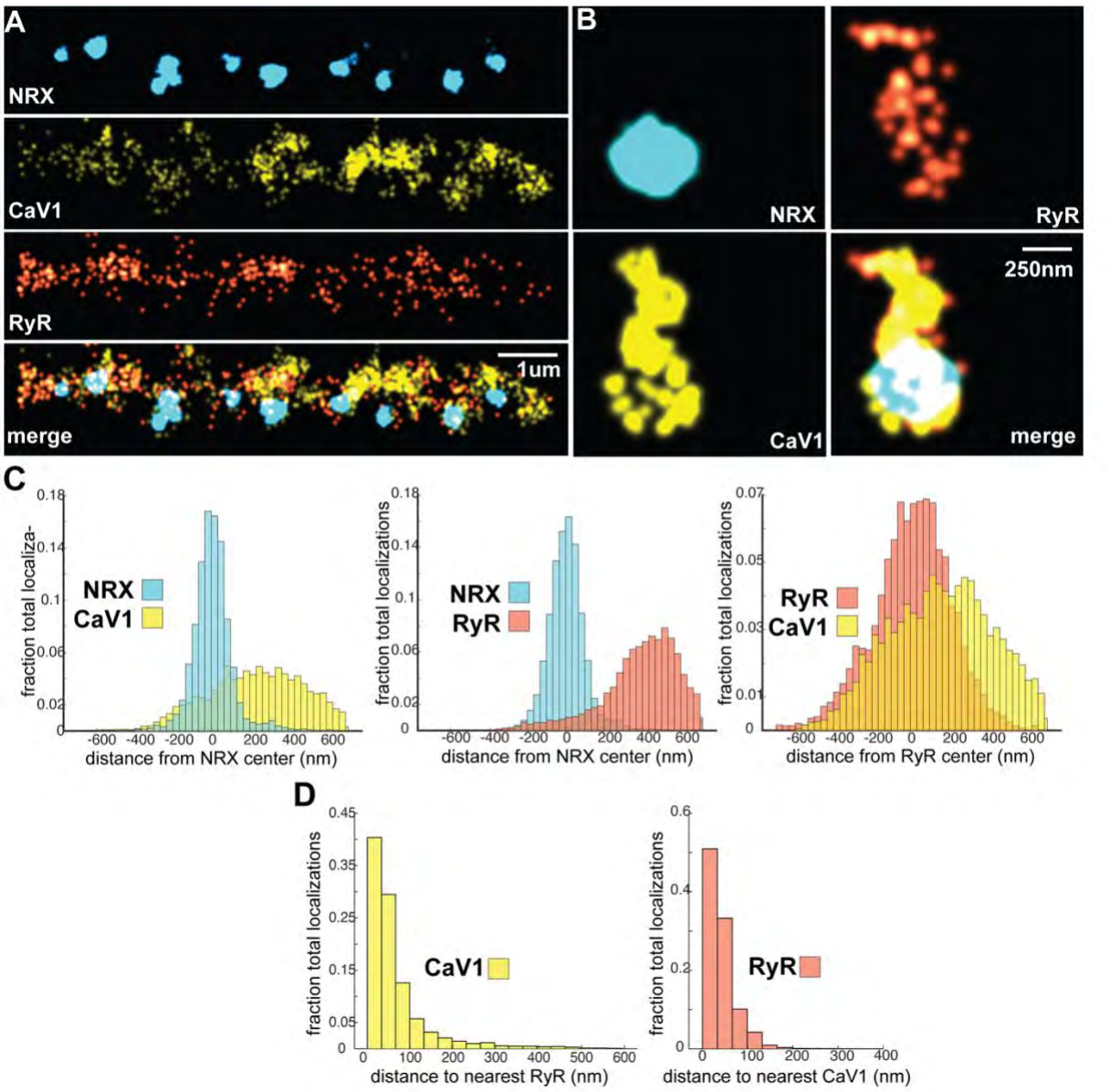

Figure 5. CaV1/RyR colocalize to form a lateral calcium source.

(a) CaV1 and RyR colocalize throughout the dorsal cord. Dorsal cord images: active zones labeled by Neurexin/*nrx-1(ox719[SKY-S])* does not colocalize with CaV1/*egl-19(ox728[SNAP])* and RyR/*unc-68(ox721[HALO])*. Scale bar = 1um

(b) RyR and CaV1 colocalize within synapses. Single synapse region of interests: active zones labeled by Neurexin/*nrx-1(ox719[SKY-S])* does not colocalize with CaV1/*egl-19(ox728[SNAP])* and RyR/*unc-68(ox721[HALO])*. Scale bar = 250nm.

(c) Cumulative frequency distribution plot of distances from CaV1/*egl-19(ox728[SNAP])* localization to Neurexin/*nrx-1(ox719[SKY-S])* cluster center measured from single synapses. Cumulative frequency distribution plot of distances from RyR/*unc-68(ox721[HALO])* localization to Neurexin/*nrx-1(ox719[SKY-S])* cluster center measured from single synapses. Cumulative frequency distribution plot of distances from CaV1/*egl-19(ox728[SNAP])* localization to RyR/*unc-68(ox721[HALO])* measured from single synapses.

(d) RyR/*unc-68(ox721[HALO])* and CaV1/*egl-19(ox728[SNAP])* are coincident. Nearest neighbor analysis was performed on CaV1 localizations to find the nearest RyR localization. Nearest neighbor analysis was performed on RyR/*unc-68(ox721[HALO])* localizations to find the nearest CaV1/*egl-19(ox728[SNAP])* localization. n=5 animals, 25 synapses

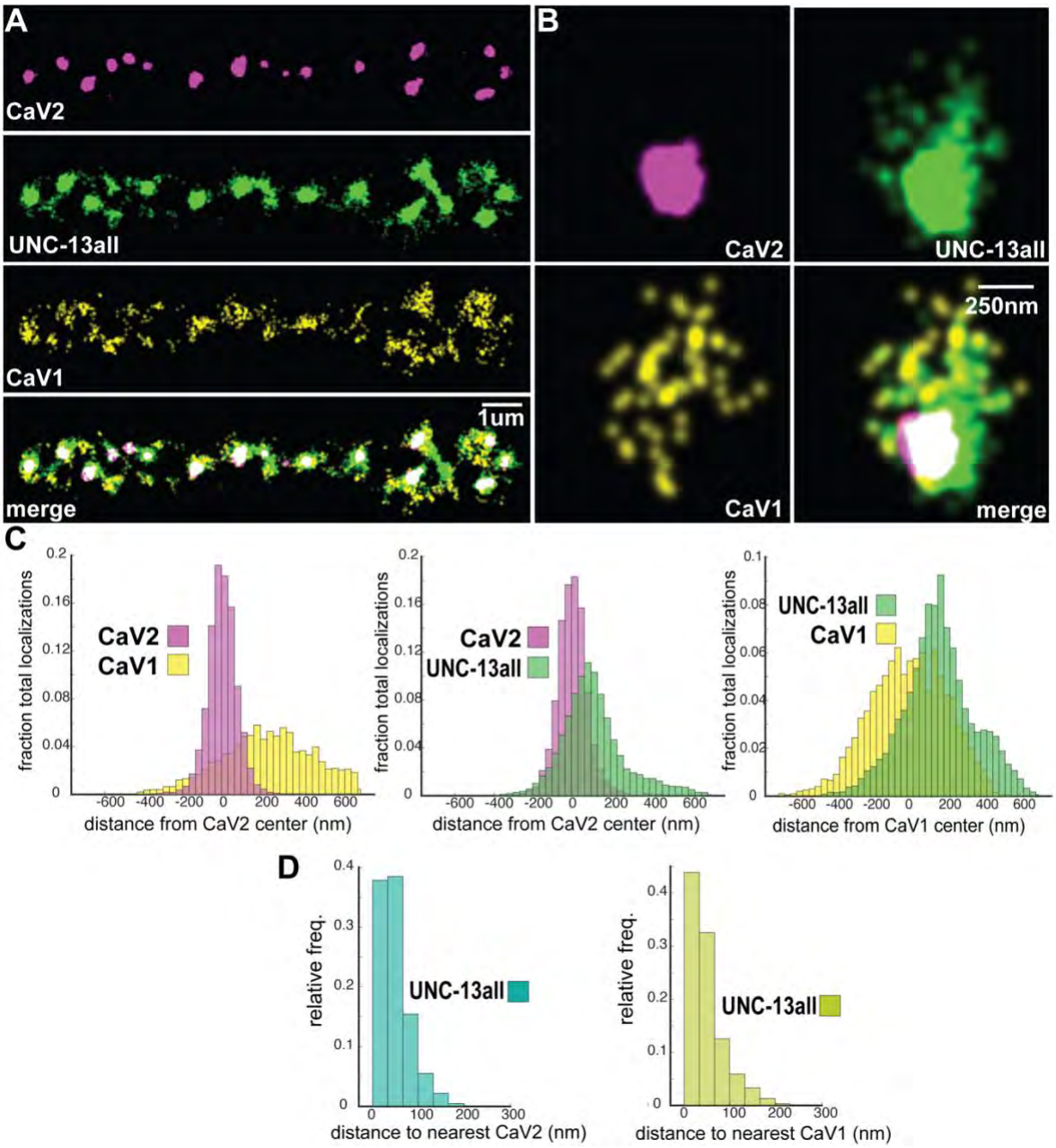

Figure 6. UNC-13all localizes with CaV2 and CaV1 calcium channels.
Localization microscopy identifies CaV1 and CaV2 associated with *unc-13(ox748[SKY-S])* which labels a c-terminal site common to all isoforms.
(A) UNC-13all colocalizes with both CaV1 and CaV2 throughout the dorsal cord. Localization microscopy images of dorsal nerve cord labelled with CaV2/*unc-2(ox672[HALO])*, CaV1/*egl-19(ox728[SNAP])*, and *unc-13(ox748[SKY-S])*. Animals stained with HTL-JF646 and STL-JF549.
(B) UNC-13all colocalizes with both CaV1 and CaV2 within single synapses. Single synapse region of interests labelled with CaV2/*unc-2(ox672[HALO])*, CaV1/*egl-19(ox728[SNAP])* and *unc-13(ox748[SKY-S])*.
(C) Cumulative frequency distribution plot of distances from CaV1/*egl-19(ox728[SNAP])* localization to CaV2/*unc-2(ox672[HALO])* cluster center. Distance from *unc-13(ox748[SKY-S])* localizations to CaV2/*unc-2(ox672[HALO])* cluster center measured from single synapses.
(D) Nearest-neighbor distances between CaV1/*egl-19(ox728[SNAP])* and *unc-13(ox748[SKY-S])* localizations. Nearest neighbor analysis between *unc-13(ox748[SKY-S])* and CaV2/*unc-2(ox672[HALO])* or CaV1/*egl-19(ox728[SNAP])*.

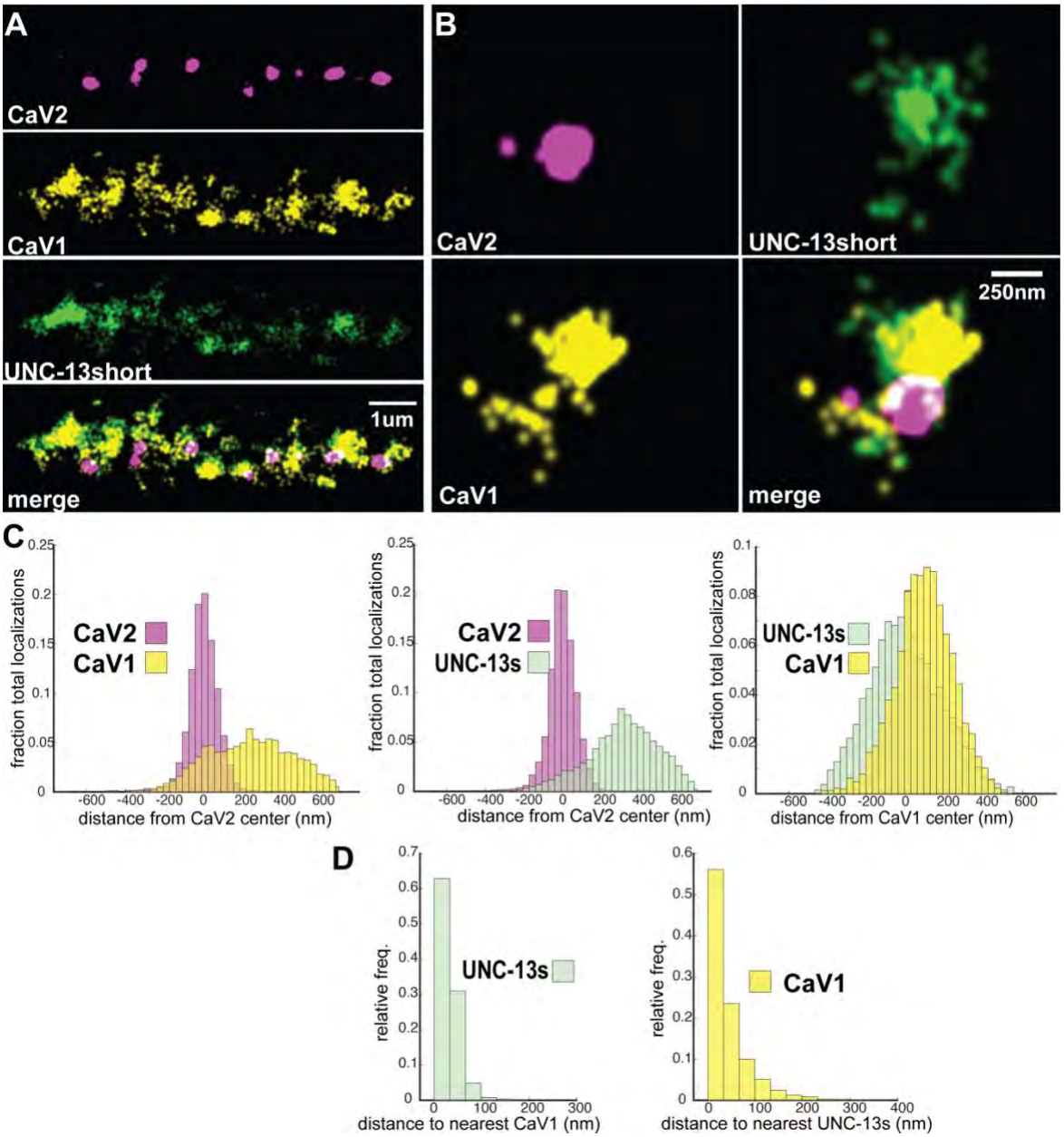

Figure 7. UNC-13s localizes with CaV1 but not CaV2 calcium channels.

Localization microscopy identifies CaV1 associated with *unc-13(ox814[SKY-S])* which labels a n-terminal site common to a short isoform.

(a) UNC-13short colocalizes with CaV1 throughout the dorsal cord. Dorsal cord images labelled with CaV2/*unc-2(ox672[HALO])*, CaV1/*egl-19(ox728[SNAP])* and UNC-13s/*unc-13(ox814[SKY-S])*. Animals stained with HTL-JF646 and STL-JF549.

(b) UNC-13short colocalizes with CaV1 within a single synapse. Single synapse region of interests: images labelled with CaV2/*unc-2(ox672[HALO])*, CaV1/*egl-19(ox728[SNAP])* and UNC-13s/*unc-13(ox814[SKY-S])*. Animals stained with HTL-JF646 and STL-JF549.

(c) Cumulative frequency distribution plot of distances from CaV1/*egl-19(ox728[SNAP])* localization to CaV2/*unc-2(ox672[HALO])* cluster center. Cumulative frequency distribution plot of distance from UNC-13s/*unc-13(ox814[SKY-S])* localizations to CaV2/*unc-2(ox672[HALO])* cluster center was measured from single synapses. Distance from UNC-13s/*unc-13(ox814[SKY-S])* localizations to CaV1/*egl-19(ox728[SNAP])* cluster center was measured from single synapses.

(d) Nearest-neighbor distances between CaV1/*egl-19(ox728[SNAP])* and UNC-13s/*unc-13(ox814[SKY-S])* localizations. Nearest neighbor analysis between UNC-13s/*unc-13(ox814[SKY-S])* and CaV1/*egl-19(ox728[SNAP]).*

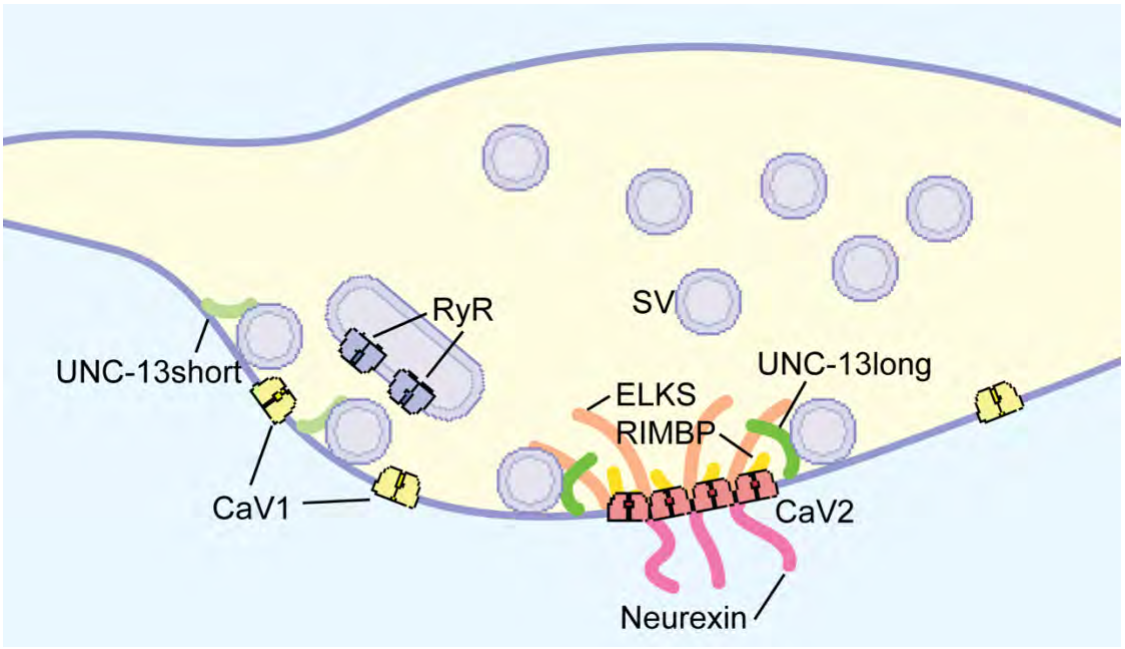

Figure 8. Two sites of fusion for synaptic vesicles

Voltage gated calcium channels at the neuromuscular presynapse of C. elegans localize to two distinct areas. CaV2 localizes to the dense projection along with ELKS, RIMBP, Neurexin, CaV2 and UNC-13L. Here, CaV2 is required to fuse a near pool of synaptic vesicles which dock within 100nm of the dense projection. The second, lateral site is centered at 300nm away from the dense projection but can span hundreds of nanometers. CaV1 localizes to the lateral site, along with ryanodine receptor. Here, CaV1 and RyR are required to fuse a lateral pool of vesicles which dock >100nm from the dense projection. These near and far pools utilize specific release machinery. Most UNC-13all localizes to the dense projection. However, some UNC-13 localizes with CaV1 at the lateral site. Isoform specific tagging shows UNC-13S localized with lateral site.

Table S1: Viability of calcium channel mutants.

viability	+	+	–	+	+	–	–	+	+
genotype CaV2 CaV1 RyR	+ + +	CaV2(-) + +	+ CaV1(-) +	+ CaV1(Δns) +	+ + RyR(-)	CaV2(-) + RyR(-)	CaV2(-) CaV1(Δns) +	CaV2(Δnmj) CaV1(Δns) +	+ CaV1(Δns) RyR(-)
strain	N2	AQ130	n/a	EG9034	CB540	n/a	n/a	EG9406	EG8827

88

allele	gene	sgRNA	Repair Template	tag	chr	terminus
ox672	*unc-2*	pSAM429 (ACAGACCGCCAACCAACCGG)	pSAM593	HALO	X	internal
ox704	*rimb-1*	TGGGTAAATCGATAAATCG	pSAM514	SKY-S	III	c
ox719	*nrx-1*	TTTTCTTTGCCACCCCATTC	pSAM534	SKY-S	V	c
ox721	*unc-68*	pSAM488 (gattagttagttccaagaaA)	pSAM593h	HALO	V	n
ox727	*ctn-1d*	CATCCAATGTAATCGGC	pSAM598	SKY-S	III	c
ox728	*egl-19*	CTTCTCATCCATTGCTC	pSAM604	SNAP	IV	internal
ox729	*syd-1*	GCACTGCGATTCCGAGACAT	pSAM545	SKY-S	II	c
ox730	*syd-2*	TTGCTGTAGCTCATatttct	pSAM549	SKY-S	X	n
ox731	*syg-1*	GGACCACTTCCGGCGACGAG	pSAM544	SKY-S	X	c
ox747	*elks-1*	gagcagtacaatATGGCACC	pSAM550	SKY-S	IV	n
ox748	*unc-13all*	gctttgaatccaacaaaaaa	pSAM613	SKY-S	I	c
ox803	*magi-1*	aagATGACCGACAAAACAGC	pSAM552	SKY-S	IV	n
ox814	*unc-13b*	GGAACTGCAAGACTTGGCAC	pSAM684	SKY-S	I	n
ox802	*unc-44*	GCTGTTGGTCGTGCTCCCGA	pSAM546	SKY-S	IV	c
ox708	*unc-44*	GCTGTTGGTCGTGCTCCCGA	pSAM557	SNAP	IV	c

89 **Table S2: Super-resolution Alleles Generated for this study.**